

2018-05

Pseudo-static tests of terminal stirrup-confined concrete-filled rectangular steel tubular columns

Ding, FX

<http://hdl.handle.net/10026.1/10996>

10.1016/j.jcsr.2018.01.017

Journal of Constructional Steel Research

Elsevier

All content in PEARL is protected by copyright law. Author manuscripts are made available in accordance with publisher policies. Please cite only the published version using the details provided on the item record or document. In the absence of an open licence (e.g. Creative Commons), permissions for further reuse of content should be sought from the publisher or author.

1 This paper is published on:

2 Journal of Constructional Steel Research, Volume 144, May 2018, P135-152.

3 Pseudo-static tests of terminal stirrup-confined concrete-filled 4 rectangular steel tubular columns

5 Fa-xing Ding ^{a,b}, Liang Luo ^{a,*}, Liping Wang ^a, Shanshan Cheng ^c, Zhi-wu Yu ^{a,b}

6 ^a School of Civil Engineering, Central South University, Changsha, China.

7 ^b Engineering Technology Research Center for Prefabricated Construction Industrialization of Hunan
8 Province, Changsha, China.

9 ^c School of Engineering, University of Plymouth, United Kingdom.

10 *Corresponding author, Ph.D., E-mail: luoliang1220@csu.edu.cn

11
12 **ABSTRACT:** This paper mainly presents a pseudo-static test program on 12 terminal stirrup-confined square
13 concrete-filled steel tube (SCFT) columns and 14 rectangular SCFT columns under constant axial pressure. The
14 effects of various factors on the hysteretic behavior of specimens are investigated. These factors include with or
15 without stirrups, height of terminal stirrup region, equivalent stirrup ratio, stirrup form, loading direction,
16 height-length ratio (L/B), length-width ratio (B/D), axial compression ratio (n) and sliding support. The failure
17 mode, strain ratio, hysteretic curve, skeleton curve, ultimate bearing capacity, ductility, stiffness degradation,
18 energy dissipation, as well as the residual deformation of the specimens are analyzed. The results indicate that:
19 (1) When n is relatively larger, the bidirectional stirrups can effectively delay the local buckling of steel tube
20 and greatly increase the ultimate bearing capacity, stiffness, equivalent damping viscosity index, residual
21 deformation rate and ductility index, and further significantly improve the seismic behavior of the rectangular
22 SCFT columns; (2) Axial pressure can improve the confinement effect from the steel tube to the core concrete,
23 also bidirectional stirrups can directly confine the core concrete to decrease strain ratio of the steel tube; (3)
24 With the same value of n , increasing the height of terminal stirrup region or increasing the equivalent stirrup
25 ratio can effectively improve the seismic behavior of the rectangular SCFT columns; (4) The influence of
26 loading direction, L/B and B/D on the ductility of rectangular SCFT columns are not obvious.

27
28 **Keywords:** Rectangular concrete-filled steel tubular column; Terminal stirrup; Pseudo-static test; Seismic
29 behavior; Ultimate bearing capacity; Ductility index

30 1. Introduction

31 Concrete filled steel tubular (CFT) columns have been increasingly used in bridges and high-rise
32 buildings due to their enhanced compressive strength and stiffness, improved ductility and higher energy
33 absorption capacity compared to the conventional steel or concrete structures. With such benefits, the use
34 of CFT columns is becoming more commonplace and the performance of CFT columns has caught more
35 and more research attention [1-9]. Several studies have demonstrated that circular CFT stub columns can
36 provide sufficient constraint from the steel tube to the core concrete [1-4]. However, the flexural rigidity
37 and flexural capacity are comparatively low and, in particular, the configuration of joints connecting the
38 circular CFT columns and beams is complex. In comparison, the confining effect from the steel tube to the
39 core concrete in square or rectangular CFT columns is relatively weak, despite that the section moment of
40 inertia (therefore bending stiffness) is improved and the joint configuration is more convenient [5-9].
41 However, the confining effect from the steel tube to the concrete in rectangular CFT columns is relatively
42 weak and the load-bearing capacity and ductility under seismic action are therefore reduced. The seismic
43 behavior of rectangular CFT members is increasingly becoming a critical problem in the engineering field
44 [10-12].

45 Pseudo-static tests are usually used to study the seismic performance of CFT columns, that is, axial
46 compression and lateral cyclic load are applied to columns simultaneously. Amit H. Varma et al. [10]
47 conducted a pseudo-static test study on 8 square CFT columns to investigate the effects of parameters
48 include width to thickness ratio, steel yield strength and axial compression ratio n on the seismic behavior
49 of such members. The experimental results show that there is no obvious difference of the displacement
50 ductility index when the steel ratio of cross section is changed from 7.5% to 11.0%. Also, when n is 0.21,
51 the displacement ductility index of conventional steel specimens is not obviously different from high
52 strength steel specimens. Similarly, Liu et al. [11] conducted a seismic behavior test study on 9 square CFT
53 columns with the steel ratio ranged from 6.9% to 12.4% under constant axial load and lateral cyclic load.
54 Effects of n , width to thickness ratio, height-length ratio and concrete strength on the ductility and energy
55 dissipation ability were studied. Han et al. [12] focused on ultimate bearing capacity and ductility on 12
56 square CFT columns and 18 rectangular CFT columns with the steel ratio during 8.6%~14.5% under a
57 pseudo-static test study. Three key parameters including n , length-width ratio and core concrete strength
58 were considered in the experimental study. The results from the above studies reflected that when n is
59 more than 0.5, the ductility and energy dissipation of the square CFT columns and rectangular CFT
60 columns are generally low.

61 Moreover, many researchers have proposed different structural measures on square CFT columns in
62 order to increase the confinement effect from the steel tube to the core concrete and improve their seismic
63 performance. These structural measures include steel jacket welded outside the steel tube [13], encased
64 profile steel [14], longitudinal stiffening ribs [15] and horizontal binding bars [16] arranged inside the steel
65 tube. Mao et al. [13] proposed 3 forms of steel jackets welded to the potential plastic hinge region to delay
66 the local buckling of the steel tube and ensure a ductile behavior of CFT members. However, due to the
67 limitation of welding technology, the improvement of ultimate bearing capacity and stiffness is not obvious.
68 The structural measures outside the steel tube are mainly applied to the reinforcement of the existing CFT
69 members. On the other hand, for the new CFT members, increasing the internal steel is usually applied to
70 improve the steel ratio. For example, Zhu et al. [14] proposed profile steel embedded in core concrete to
71 prevent the fracture surface of concrete under failure load. When the equivalent amount of steel is
72 increased by 97.8%, ultimate bearing capacity, displacement ductility index, energy-dissipation index are
73 increased by 9.5%, 15.4%, 13.5%. Zhang et al. [15] proposed longitudinal stiffening ribs on 2 inner faces or
74 4 inner faces of square steel tubes. It was found that when n is 0.4 and 0.5, compared to the specimen of 2
75 stiffening ribs, the specimen with 4 stiffening ribs have no obvious improvement in the ultimate bearing

76 capacity compared to the specimen with 2 stiffening ribs. However, its displacement ductility index is
77 increased by 30%. Wang et al. [16] proposed a measure by bolting horizontal binding bars inside the
78 square steel tubes to postpone their local buckling and improve the seismic behavior of CFT specimens.
79 The results show that when n is 0.2, the ultimate bearing capacity is almost unchanged while the ductility
80 index is increased by 67%. Moreover, when n is 0.6, the ultimate bearing capacity is increased by 10% and
81 the ductility index is increased by 30%.

82 However, it is difficult to perform the welding work for large-dimensional CFT columns due to their too
83 thick steel tube in practical project. Consequently, the thin-walled rectangular CFT columns have been widely
84 used. However, the latters' low steel ratio will weaken their seismic performance. In order to improve the axial
85 compressive performance of thin-walled square CFT stub columns, Ding *et al.* [17] conducted a comparison
86 study of four structural measures including studs, circular stirrups, rhombus stirrups and bidirectional
87 stirrups, based on which they proposed a way of welding the bidirectional stirrups to the inner wall of the
88 square steel tube. This method was proved to exert the most effective constraint on the core concrete and
89 hence was applied to round-ended CFT stub columns under axial compression [18]. Similarly, it can also
90 be applied to the rectangular CFT columns for the study on seismic performance.

91 It is known that the weak region of a CFT frame column is located at its terminal section, the idea of
92 stirrups encryption in joint area of reinforced-concrete structure can be applied to CFT columns. In order to
93 reduce the amount of steel, improve the economic efficiency and optimize the construction, the authors put
94 forward the terminal stirrup-confined rectangular CFT (SCFT) columns in which the bidirectional stirrups
95 are welded inside the rectangular steel tube at the columns ends with large bending moment. For
96 large-dimensional CFT columns, it is convenient for operators entering the steel tube and welding stirrups
97 only at the columns ends.

98 In conventional standards, storey height and storey number are limited in order to limit n of the
99 columns and ensure their seismic performance. However, in actual high-rise and super high-rise buildings,
100 n of columns is often very large, even reaching 0.8. The aim of this study, therefore, is to focus on the
101 advantage of rectangular SCFT columns under high n even up to 0.8. More specifically, two objectives are
102 included in this study: (1) to investigate the seismic behavior of rectangular SCFT columns through a
103 pseudo-static test study on 26 specimens; (2) to study the effects of 9 main factors on the hysteretic behavior
104 of specimens include with or without stirrups, height of terminal stirrup region, equivalent stirrup ratio,
105 loading direction, height-length ratio (L/B), length-width ratio (B/D), axial compression ratio (n) and sliding
106 support.

107

108 **2. Experimental investigation**

109 **2.1 Specimens and materials**

110 In this test program, 26 specimens were designed, including 12 square SCFT columns and 14
111 rectangular SCFT columns. Each specimen consisted of concrete filled steel tubular column, top plate,
112 bottom plate and stiffening ribs. Fig. 1 and Fig. 2 exhibit a schematic view and the actual photos of the
113 specimens, respectively. The details of the labels and parameters of specimens are listed in Table 1. In the
114 label of specimen, the first letter "s" or "r" represents square or rectangle, the second letter "c" means
115 column, the third letter "h" indicates that the loading mode is hysteretic. B is the length (longer side) of
116 rectangular section, D is the width (shorter side) of the rectangular section, t is the wall thickness of the
117 steel tube, L is the effective height of column excluding the height of stiffening ribs. ρ_s is the steel ratio of
118 the cross section, calculated by $\rho_s = A_s / (A_s + A_c)$, where A_s and A_c are the area of steel tube and core concrete,
119 respectively. a_s , b_s and d_s are horizontal spacing, longitudinal spacing and diameter of stirrups, respectively.
120 h_1 and h_2 are height of terminal stirrup region at the bottom and top of specimens. Stirrups of h_1 mainly
121 bear the bending moment and shear force, while stirrups of h_2 are constructional reinforcement to prevent

122 the core concrete from premature crushing failure. f_{cu} is the cubic compressive strength of concrete, f_c is
 123 uniaxial compressive strength of concrete prism. According to Ding *et al.* [19], the conversion relationship
 124 between f_c and concrete compressive strength f_{cu} is $f_c=0.4f_{cu}^{7/6}$. f_s and f_{sv} is the yield strength of steel tube
 125 and stirrup, respectively. ρ_{sa} is equivalent stirrup ratio defined as $\rho_{sa}=\rho_{sv}\times f_{sv}/f_s$, where ρ_{sv} is the stirrup ratio.
 126 n is axial compression ratio, calculated by $n=N/N_u$, where N is the constant axial pressure and N_u is the
 127 nominal bearing capacity. N_u is obtained from formula $N_u=f_cA_c+f_yA_s$ [11, 15, 16]. P^+ and P^- are the
 128 maximum positive and negative horizontal bearing capacity. DI is the displacement ductility index
 129 obtained from the average value of positive and negative displacement ductility index. K_1 is the initial
 130 stiffness obtained from the average value of positive and negative initial stiffness.

131 Among these specimens, sch1 and sch3 are without stirrups while the others are with bidirectional
 132 stirrups on the cross-sections of specified spacing. Besides, sch1, sch2 and sch5 were tested without sliding
 133 support because the n of sch1, sch2 is 0 and sch5 is used to compare the effect of sliding support with sch3.
 134 Moreover, the stirrup diameter of sch8 is 8 mm and sch9 is with ring stirrups. Particularly, the n of
 135 rch1~4-0.8 is up to 0.8.

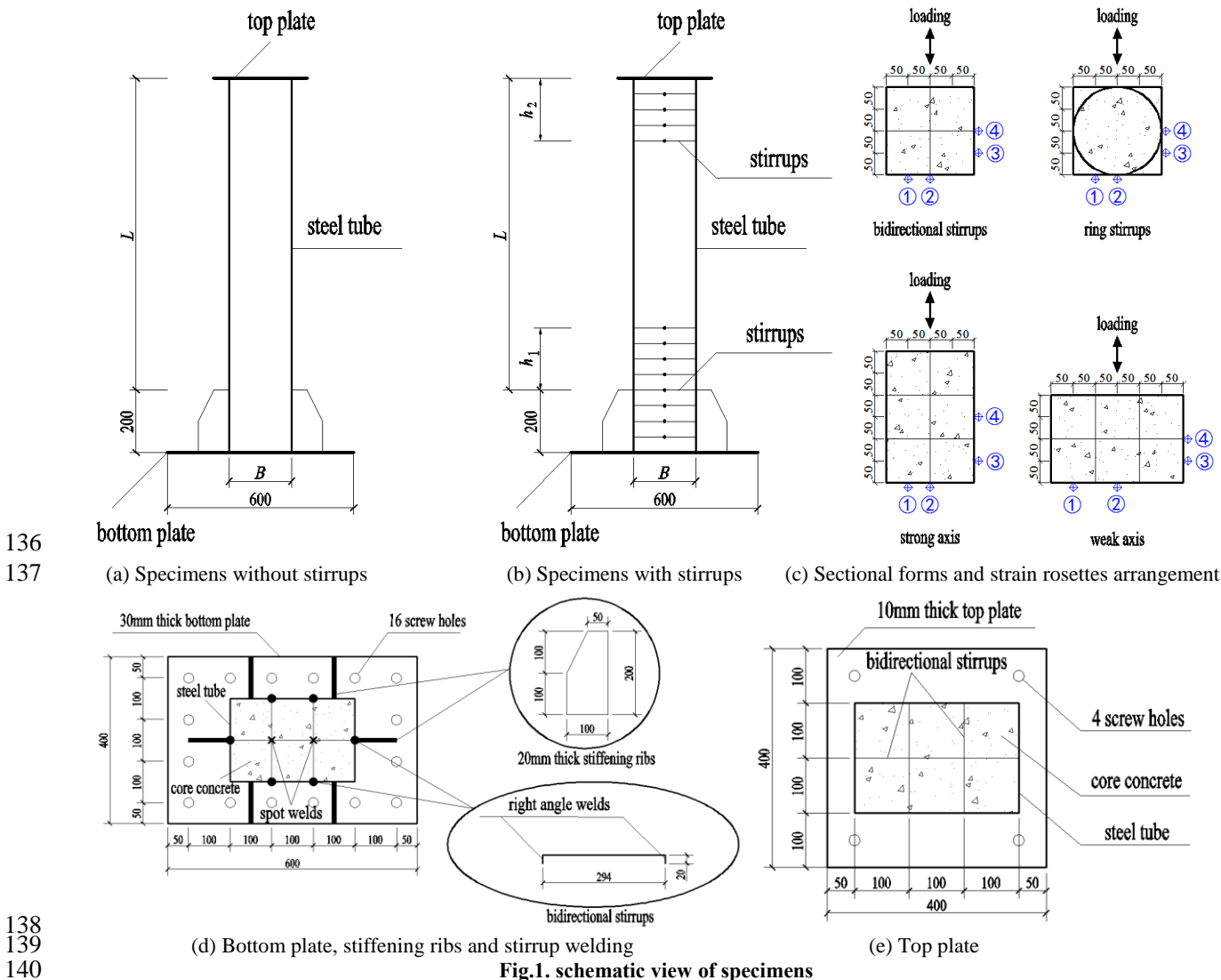
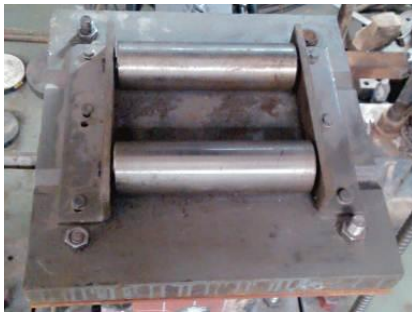
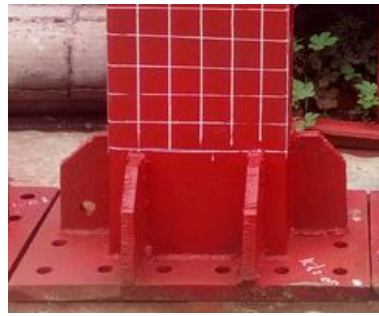


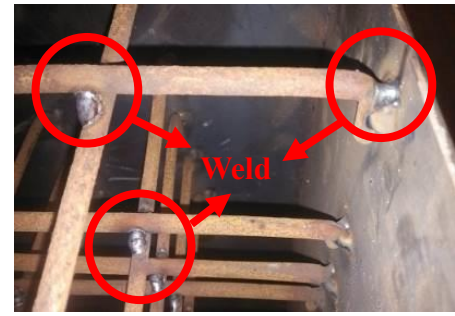
Fig.1. schematic view of specimens



(a) Top plate and sliding support



(b) Bottom plate and stiffening ribs



(c) Stirrup welding

Fig.2. Actual diagram of specimens

Table 1 Parameters of specimens

(a) Square SCFT columns

Specimen	$B \times D \times t \times L$ /mm	ρ_s	a_s /mm	b_s /mm	d_s /mm	h_1	h_2	f_{cu} /MPa	f_c /MPa	f_s /MPa	f_{sv} /MPa	ρ_{sa}	n	N /kN	sliding support	P^+ /kN	P^- /kN	DI	K_1 /(kN/mm)
sch1	200×200×3×1500	0.06	-	-	-	0	0	43.2	32.4	368	285	-	0	0	without	54.62	53.96	5.02	3.50
sch2	200×200×3×1500	0.06	100	50	6	200	200	43.2	32.4	368	285	0.45%	0	0	without	56.36	57.27	6.12	3.75
sch3	200×200×3×1500	0.06	-	-	-	0	0	43.2	32.4	368	285	-	0.4	835.7	with	61.02	58.54	3.74	4.11
sch4	200×200×3×1500	0.06	100	50	6	200	200	43.2	32.4	368	285	0.45%	0.4	835.7	with	70.15	68.48	4.38	4.27
sch5	200×200×3×1500	0.06	100	50	6	0	0	43.2	32.4	368	285	0.45%	0.4	835.7	without	66.28	66.81	3.35	3.87
sch6	200×200×3×900	0.06	100	50	6	200	200	43.2	32.4	368	285	0.45%	0.4	835.7	with	95.71	96.88	4.71	17.63
sch7	200×200×3×1500	0.06	100	50	6	400	200	43.2	32.4	368	285	0.45%	0.6	1253.6	with	52.03	50.34	2.85	5.08
sch8	200×200×3×1500	0.06	100	50	8	400	200	43.2	32.4	368	504	1.42%	0.6	1253.6	with	83.54	79.39	3.02	5.76
sch9	200×200×3×1500	0.06	ring	50	6	400	200	43.2	32.4	368	285	0.73%	0.6	1253.6	with	48.40	47.23	2.38	4.68
sch10	200×200×3×2000	0.06	100	50	6	200	200	43.2	32.4	368	285	0.45%	0.2	417.9	with	47.58	45.29	4.62	1.92
sch11	200×200×3×2000	0.06	100	50	6	200	200	43.2	32.4	368	285	0.45%	0.4	835.7	with	49.70	49.28	4.08	2.12
sch12	200×200×3×2000	0.06	100	50	6	400	200	43.2	32.4	368	285	0.45%	0.6	1253.6	with	47.81	48.51	2.63	2.43

(b) Rectangular SCFT columns

Specimen	$B \times D \times t \times L$ /mm	ρ_s	a_s /mm	b_s /mm	d_s /mm	h_1	h_2	f_{cu} /MPa	f_c /MPa	f_s /MPa	f_{sv} /MPa	ρ_{sa}	n	N /kN	sliding support	P^+ /kN	P^- /kN	DI	K_1 /(kN/mm)
rch1	300×200×3×1500	0.05	100	50	6	300	200	43.2	32.4	368	285	0.52%	0.2	587.7	with	147.78	157.65	4.54	8.34
rch2	300×200×3×1500	0.05	100	50	6	300	200	43.2	32.4	368	285	0.52%	0.4	1175.5	with	134.96	135.94	4.27	9.85
rch3	300×200×3×1500	0.05	100	50	6	300	200	43.2	32.4	368	285	0.52%	0.7	2057.1	with	117.59	126.28	2.26	12.41
rch4	300×200×3×1500	0.05	100	50	6	600	200	43.2	32.4	368	285	0.52%	0.7	2057.1	with	128.90	133.90	2.67	13.52
rch5	200×300×3×1500	0.05	100	50	6	300	200	43.2	32.4	368	285	0.52%	0.2	587.7	with	110.56	113.16	4.83	5.52
rch6	200×300×3×1500	0.05	100	50	6	300	200	43.2	32.4	368	285	0.52%	0.7	2057.1	with	84.75	86.96	2.48	6.77
rch7	200×300×3×1000	0.05	100	50	6	300	200	43.2	32.4	368	285	0.52%	0.7	2057.1	with	165.23	162.11	2.75	14.28
rch8	300×200×3×2000	0.05	100	50	6	300	200	43.2	32.4	368	285	0.52%	0.2	587.7	with	117.00	117.69	4.12	6.27
rch9	300×200×3×2000	0.05	100	50	6	300	200	43.2	32.4	368	285	0.52%	0.4	1175.5	with	107.89	104.54	3.85	6.82
rch10	300×200×3×2000	0.05	100	50	6	600	200	43.2	32.4	368	285	0.52%	0.6	1763.2	with	105.61	106.34	2.47	5.71
rch1-0.8	300×200×3×1000	0.05	100	-	-	-	-	43.5	32.6	355	-	-	-	2329.2	with	268.47	226.81	2.07	23.37
rch2-0.8	300×200×3×1000	0.05	100	50	8	600	200	43.5	32.6	355	444	1.49%	0.8	2329.2	with	328.69	316.57	3.71	41.70
rch3-0.8	300×200×3×1000	0.05	100	50	10	300	200	43.5	32.6	355	532	2.79%	0.8	2329.2	with	338.66	343.17	3.70	39.79
rch4-0.8	300×200×3×1000	0.05	100	50	10	600	200	43.5	32.6	355	532	2.79%	0.8	2329.2	with	377.69	364.96	4.17	43.98

For each specimen, the steel tube was welded from two right angle tubes which were firstly bent using the Q235 hot-rolled steel plates. The welding was performed according to the standard GB 50017-2003 [20] and the ends of the steel grooves (as the sites of welding) were kept smooth after welding. Both ends of

150 stirrups were firstly bent to right angle with bent length of 20 mm and then welded to the two ends of the
151 steel tubes in a certain range. Moreover, spot welds were adopted at the intersections of bidirectional
152 stirrups and thus they form a steel mesh.

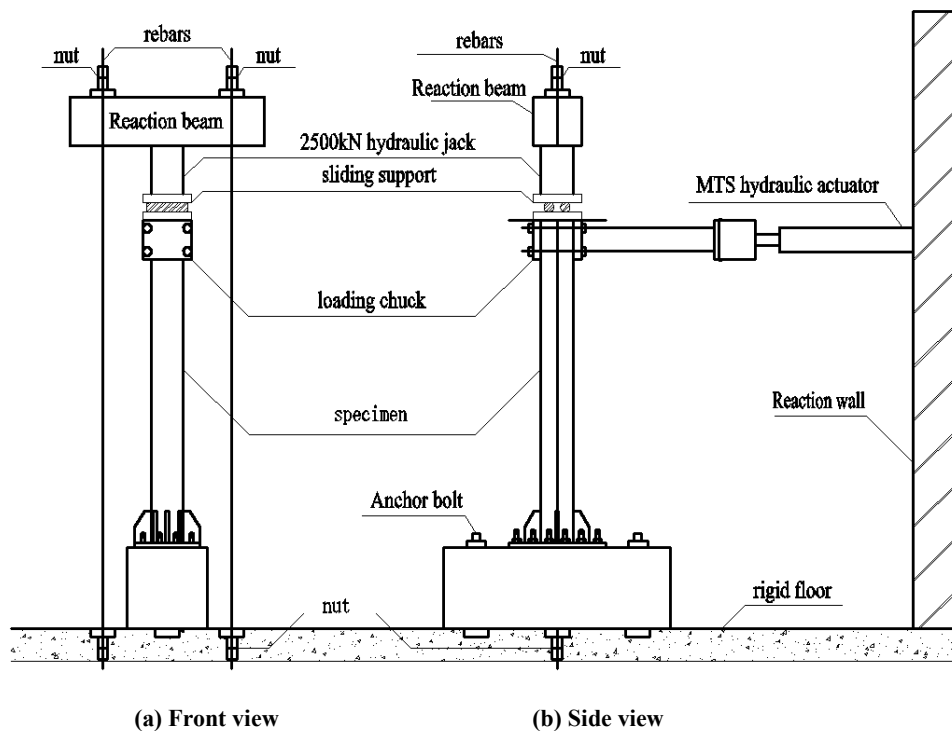
153 The bottom plate and stiffening ribs were welded to the bottom of the steel tube. Then the concrete was
154 pumped into the tube from the top and was vibrated to be well compacted. The commercial concrete of
155 grade C40 was adopted for all the specimens. Moreover, 9 standard concrete cubes with a dimension of
156 150 mm × 150 mm × 150 mm were prepared and cured at the same condition as those of SCFT specimens.
157 After 28 days of curing, the concrete had hardened completely and achieved its compressive strength. Then
158 the cover plate was welded to the top of the steel tube. For the convenience of observation and record of
159 failure mode, red paint was sprayed on the external surface of the steel tube and 50 mm × 50 mm white
160 grids were plotted on the surface.

161 Before the column tests, the cubic compressive strength f_{cu} of concrete were obtained from the testing
162 of the concrete cubes according to GB/T 50081-2002 [21]. The material properties of 3 mm thick steel
163 plates and stirrups of diameter 6mm and 8 mm were obtained from the tensile coupon tests according to
164 GB/T 228-2002 [22]. The measured material properties are presented in Table 1.

165

166 2.2 Experimental setup and instrumentation

167 The pseudo-static tests on rectangular SCFT column specimens were conducted using a MTS
168 pseudo-static test system in the National Engineering Laboratory for Construction Technology of High
169 Speed Railway at Central South University. Fig. 3 and Fig. 4 present the schematic diagram and the actual
170 photos of the tests. A top plate was fixed with the sliding support by bolts and to transmit the vertical axial
171 pressure. Besides, a bottom plate was fixed with a custom-made reinforced concrete base by bolts. Then the
172 base was fixed with rigid floor through anchor bolts. The base was strictly reinforced and debugged to
173 eliminate any possible failure during testing. The vertical load was exerted to the specimens through a
174 2500 kN hydraulic jack tensioned by rebars. The oil pump was manually controlling to ensure the vertical
175 load be stable. The horizontal low cyclic load was exerted by the MTS system hydraulic actuator through
176 the loading chunk.



177

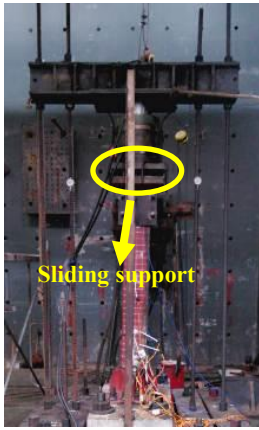
178

179

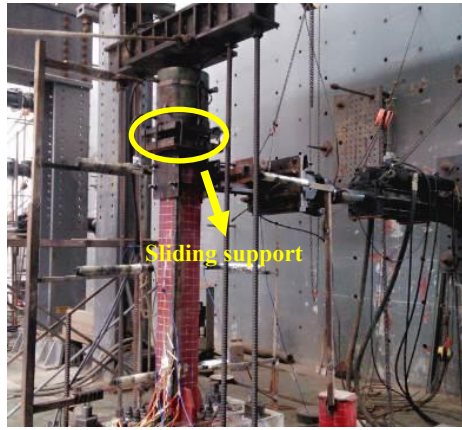
Fig.3. Schematic diagram of test

180

181



(a) Front view of sch8



(b) Side view of sch8



(c) Side view of rch1

182



(d) Front view of rch7



(e) Side view of rch1-0.8



(f) Front view of rch1-0.8

184

Fig.4. Actual diagram of test

185

186

187

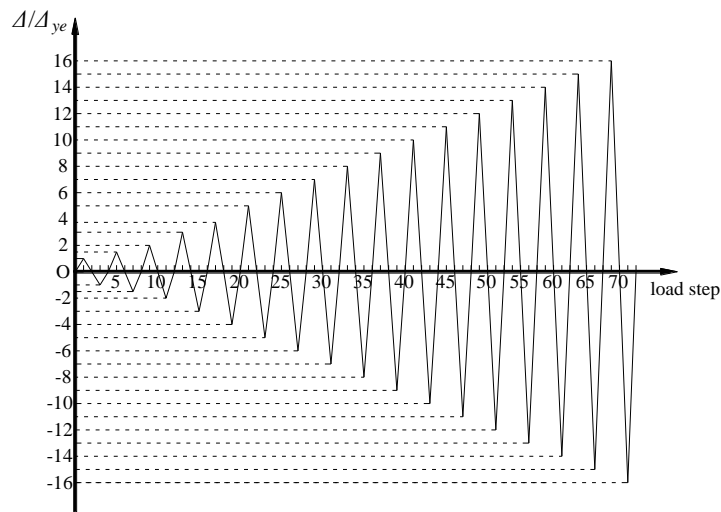
188

189

190

191

At the beginning of each test, the specimen was prepressed to a vertical load to 50% of the specified axial pressure N , then unloaded to 0, after that the specimen was loaded to N before the lateral force was applied. The axial pressure N was kept constant during the whole test. According to JG101-1996 [23], the displacement controlled method was use for horizontal cyclic loading shown in Fig.5. One loading cycle was applied for each of the peak displacement, (1, 1.5, 2, 3, 4, 5~16) Δ_y . Here Δ_y is experimental yield displacement. Such a loading procedure was attempted until the horizontal load of the specimen decreased to 85% of the horizontal bearing capacity.



192

193

Fig.5. Displacement loading system

194

195 2.3 Measuring point arrangement

196 The horizontal load, horizontal displacement and strain of steel tube were measured during the tests.
 197 The horizontal load was collected by the MTS actuator and recorded manually by the tester. Three
 198 displacement transducers with high precision were installed at three different places, namely at the same
 199 height as the horizontal loading point, half of the column height and the bottom of the specimens,
 200 respectively, to measure horizontal displacement. Moreover, four strain rosettes (S1 to S4) were placed on
 201 two adjacent surfaces at the bottom of the steel tube, as illustrated in Fig. 1 (c). The displacement and
 202 strain were acquired by a DH3818 static data measurement system. The local buckling deformation of steel
 203 tube, failure mode and failure location during the tests were also observed and recorded.

204

205 3. Experimental results and discussion

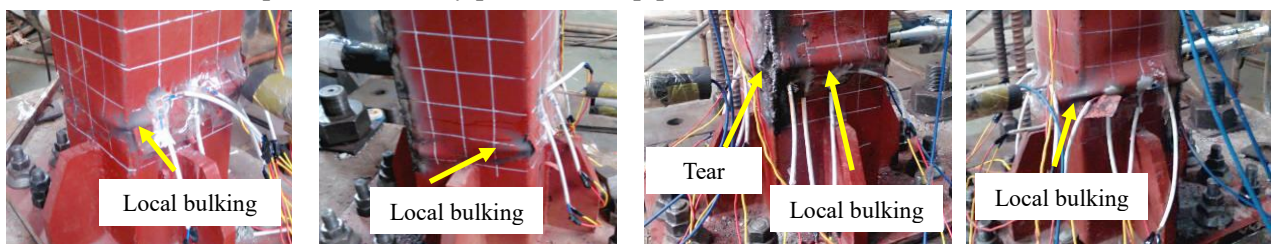
206 3.1 Damage mechanism

207 The damage process of the specimens was basically the same, which could be divided into 3 stages
 208 including elastic stage, elastic-plastic stage and failure stage. At the elastic stage of loading, the
 209 load-displacement curve of each specimen was basically linear. There was no obvious local buckling on
 210 the surface of the steel tube, and the strain was small. As the horizontal displacement increased, the
 211 specimens turned into elastic-plastic stage. The stiffness of them degraded and the load increased slowly.
 212 The steel tube displayed apparent local buckling above the stiffening ribs. As the test progressed, the range
 213 and degree of the local buckling was increasing continuously. When the horizontal load dropped below 85%
 214 of the ultimate bearing capacity, the specimens were failed. At this stage, the strain of steel tube increased
 215 rapidly with severe buckling (together with tearing at the corner of sections in some cases) in the region of
 216 stirrups and extended region of 50 mm above the stirrups. Moreover, the internal stirrups were snapped
 217 with crisp sound which indicated that the strain of stirrups reached the ultimate strain and their tensile
 218 strength was fully utilized. The final failure modes of the typical specimens are shown in Fig. 6.

219 Especially when n was up to 0.8, rch1-0.8 (without stirrups) showed obvious axial compression, the
 220 steel tube was torn with a large area along the weld, the stirrups were snapped and the core concrete was
 221 completely crushed, which is characterized by brittle failure. Unlike this, the steel tube of rch2-0.8
 222 ($\rho_{sa}=1.49\%$) displayed apparent local buckling at the bottom. Even better, only slight local buckling
 223 occurred at the bottom of rch3-0.8 ($\rho_{sa}=1.49\%$) and rch4-0.8 ($\rho_{sa}=1.49\%$). Besides, the core concrete of
 224 rch2-0.8, rch3-0.8 and rch4-0.8 was only partially crushed, which is characterized by ductile failure. These
 225 indicate that the stirrups can effectively pull the steel pipe and confine the core concrete.

226

227



(a) sch1

(b) sch2

(c) sch3

(d) sch4

228

229



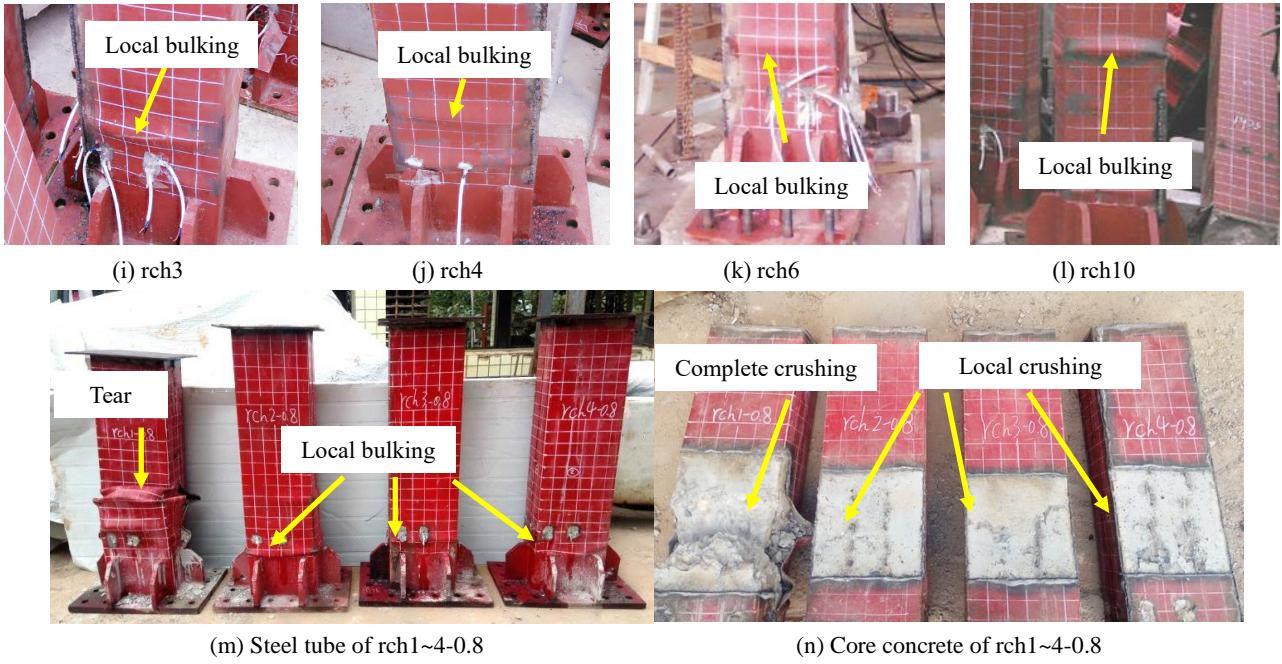
(e) sch6

(f) sch8

(g) sch12

(h) rch1

230
231



232
233
234

Fig.6. Typical failure modes of specimens

235

3.2 Load-strain ratio ($P-v_{sc}$) curves

236
237
238
239

Fig. 7 presents the load-strain ratio ($P-v_{sc}$) curves of 5 typical specimens including sch1, sch3, sch4, rch1-0.8 and rch2-0.8. As shown in Eq. (1), the v_{sc} is defined as the absolute value of ratio of circumferential strain to axial strain of the steel tube, reflecting the hoop constraint of the steel tube exerting on the core concrete [17, 24]. The larger the v_{sc} is, the stronger the hoop constraint is.

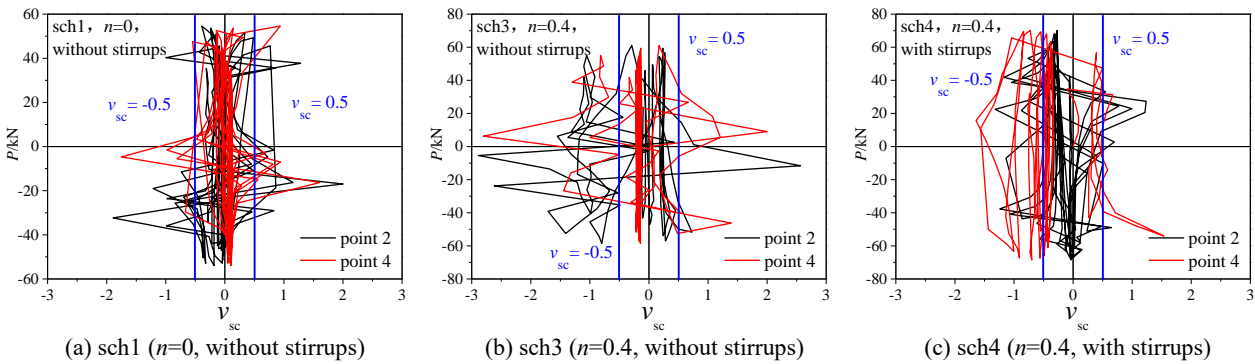
240

$$v_{sc} = \frac{\varepsilon_p}{\varepsilon_a} \quad (1)$$

241
242
243
244
245
246
247
248
249
250

As the horizontal cyclic displacement is applied, the axial strain and circumferential strain of the steel tube varies continuously, which make the strain ratio v_{sc} oscillates. Besides, the maximum v_{sc} of the 5 specimens exceeded 0.5 in the tests. The results suggest that the steel tube of all the 5 specimens exerted the hoop constraint on the core concrete. The maximum v_{sc} of 3.0 for sch3 (with $n=0.4$) is greater than that of 2.0 for the sch1 (without axial pressure). It is demonstrated that the axial pressure can increase the confining effect of the steel tube exerting on the core concrete. The maximum v_{sc} of 1.5 for sch4 (with stirrups) is less than that of 3.0 for sch3 specimen (without stirrups). Similarly, the maximum v_{sc} of 3.5 for rch2-0.8 (with stirrups) is less than that of 4.5 for rch1-0.8 (without stirrups). This indicates that the maximum v_{sc} of the steel tube is reduced due to the direct confining effect of the stirrups exerting on the core concrete.

251
252



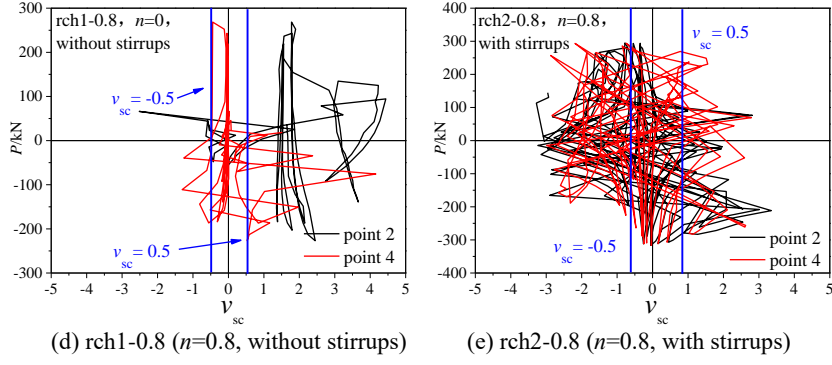


Fig.7. P - v_{sc} curve of 5 typical specimens

4. Effects of parameters on seismic behavior

4.1 Seismic behavior indexes

In this paper, 5 seismic behavior indexes are analyzed including horizontal bearing capacity P , ductility, stiffness degradation, energy-dissipation capacity and residual deformation. The horizontal bearing capacity is obtained directly from experimental results. The ductility of the specimens is expressed by the displacement ductility index DI , which is defined as the ratio of the failure displacement Δ_u over the virtual yield displacement Δ_{yv} as shown in Eq. (2):

$$DI = \frac{\Delta_u}{\Delta_{yv}} \quad (2)$$

The displacement ductility index is determined by the "General yield bending moment method" (also known as "tangent method") [25], as shown in Fig. 8. OC is the tangent of the P - Δ skeleton curve ($ODFAB$) at origin point O, P_{yv} and Δ_{yv} are the virtual yield load and the corresponding displacement, P_{max} and Δ_{max} are the ultimate load and the corresponding displacement, P_u is the horizontal failure load equal to 85% of the ultimate load in the descending range of the skeleton curve, Δ_u is the corresponding displacement. According to Eq. (2) and Fig. 8, the displacement ductility indices DI of all specimens are listed in Table 1.

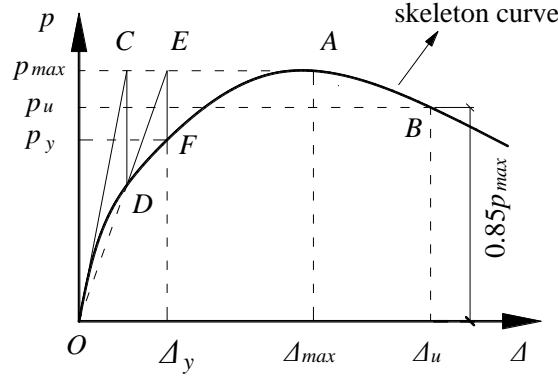


Fig.8. Ductility index obtained from general yield bending moment method

The annular stiffness K [13, 15] is used to evaluate the stiffness degradation of the specimens, which is obtained from Eq. (3):

$$K = \frac{\sum_{i=1}^n P^i}{\sum_{i=1}^n \Delta^i} \quad (3)$$

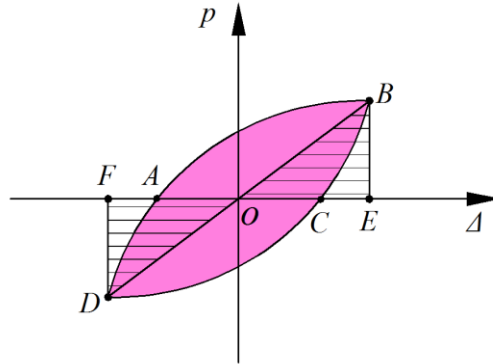
where P^i and Δ^i are respectively the peak horizontal load and the corresponding displacement of the i -th cycle, n is the total number of hysteresis loops.

The equivalent viscous damping index h_e [15, 26] is used to estimate the energy-dissipation capacity

279 of the specimens, defined as Eq. (4):

280
$$h_e = \frac{1}{2\pi} \frac{S_{ABCD}}{S_{(OBE+ODF)}} \quad (4)$$

281 where S_{ABCD} is the area of each hysteresis loop $ABCD$ (the purple area), $S_{(OBE+ODF)}$ are the total area of
 282 triangle OBE and triangle ODF (the shadow area), indicated in Fig.9.



283
 284 **Fig.9. Calculation of equivalent viscous damping index**

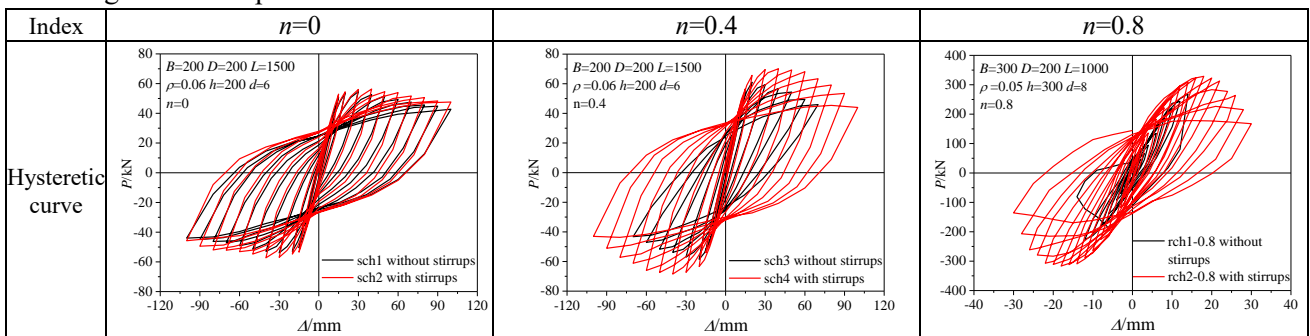
285 Residual deformation rate r [27] is defined by Eq. (5):

286
$$r = \frac{OC^i}{OE^i} \quad (5)$$

287 where OE^i and OC^i are the maximum displacement and the corresponding residual displacement of the i -th
 288 cycle, also indicated in Fig.9.

289 **4.2. Effect of stirrups**

291 Fig. 10 compares the effect of stirrups on the hysteresis behavior when n is 0, 0.4, 0.8 and the ρ_{sa} is
 292 0.45%, 0.45%, 1.49%. Table 2 lists the improvement effect of stirrups on the 5 seismic behavior indexes of
 293 the specimens. When n is 0, compared to sch1 without stirrups, the hysteresis curve of sch2 is not
 294 obviously different and its P , K_1 , maximum h_e , maximum r are only slightly improved. However, the
 295 skeleton curve of sch2 declines more slowly and the DI increased by 21.9%. When n is 0.4, compared to
 296 sch3 without stirrups, the hysteresis curve of sch4 is plumper and the skeleton curve declines more slowly.
 297 In addition, the P , K_1 , maximum h_e , maximum r are improved significantly. When n is 0.8, compared to
 298 rch1-0.8 without stirrups, all the 5 seismic behavior indexes of rch2-0.8 are improved significantly. It
 299 shows more obvious effect of stirrups on improving the hysteresis behavior of rectangular CFT columns
 300 under high axial compression ratio.



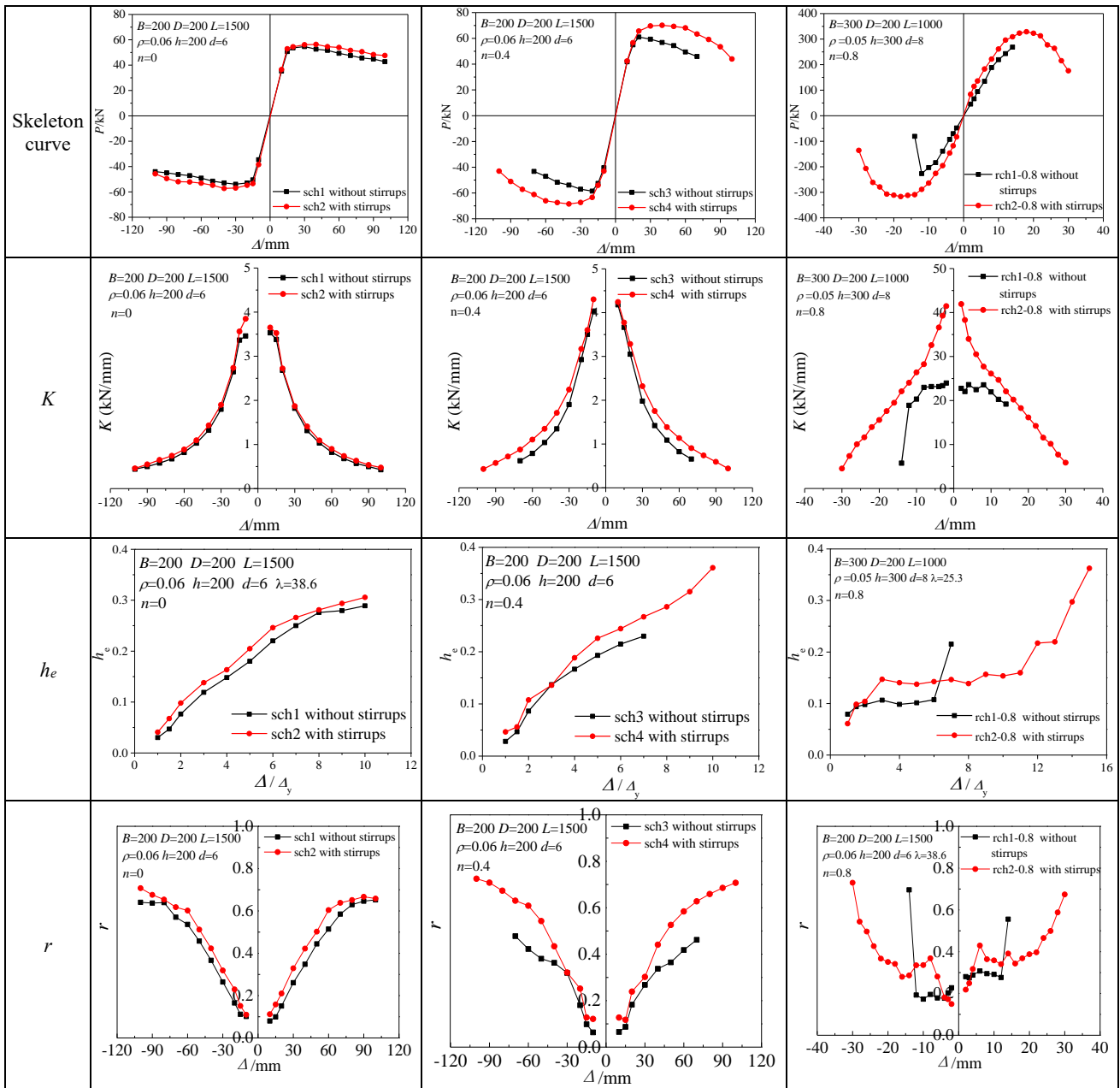


Fig.10. Influence of stirrups on hysteresis behavior when n is 0, 0.4 and 0.8

Table 2 Improved effects of stirrups on seismic behavior indexes when n is 0, 0.4 and 0.8

Indexes	$n=0$			$n=0.4$			$n=0.8$		
	sch1	sch2	Improve percentage	sch3	sch4	Improve percentage	rch1-0.8	rch2-0.8	Improve percentage
$\max(P^+, P^-)$	54.62	57.27	4.9%	61.02	70.15	15.0%	268.47	328.69	22.4%
DI	5.02	6.12	21.9%	3.74	4.38	17.1%	2.07	3.71	79.2%
K_1	3.5	3.75	7.1%	4.11	4.27	3.9%	23.37	41.70	78.4%
$\max(h_e)$	0.29	0.31	6.9%	0.23	0.36	56.5%	0.22	0.36	63.6%
$\max(r)$	0.65	0.71	9.2%	0.48	0.73	52.1%	0.56	0.73	30.4%

301

302

303

304

4.3. Effect of height of terminal stirrup region

305

Figs 11 and 12 compare the effect of height of terminal stirrup region h_1 on the hysteresis behavior when n is 0.7, 0.8 and the ρ_{sa} is 0.52%, 2.79%. It is reflected from Figs 11, 12 and Table 1 that the hysteresis loop is plumper and the skeleton curve tends to decline more slowly when the h_1 is increased from B (300mm) to $2B$ (600mm). Compared to specimen rch3, the P , DI , K_1 of rch4 are increased from 126.28 kN, 2.26, 12.5 kN/mm to 133.90 kN, 2.67, 13.5 kN/mm. On the whole, the 3 indexes are improved

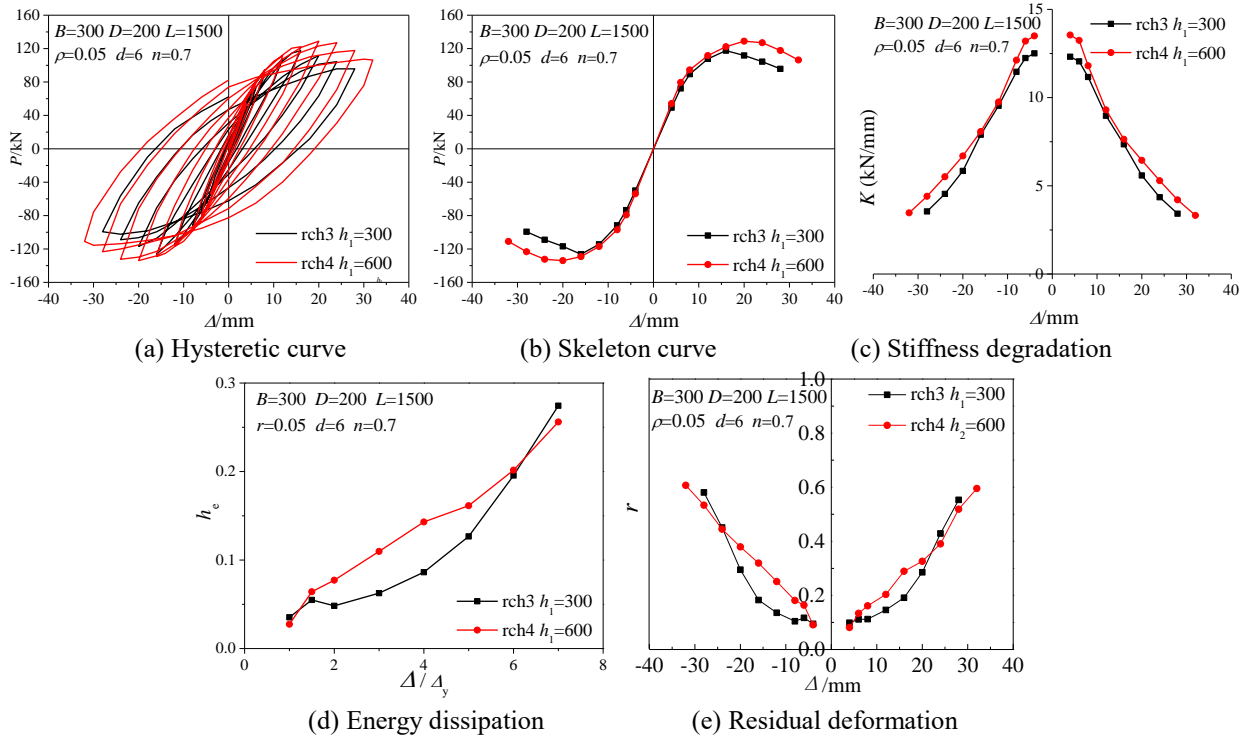
306

307

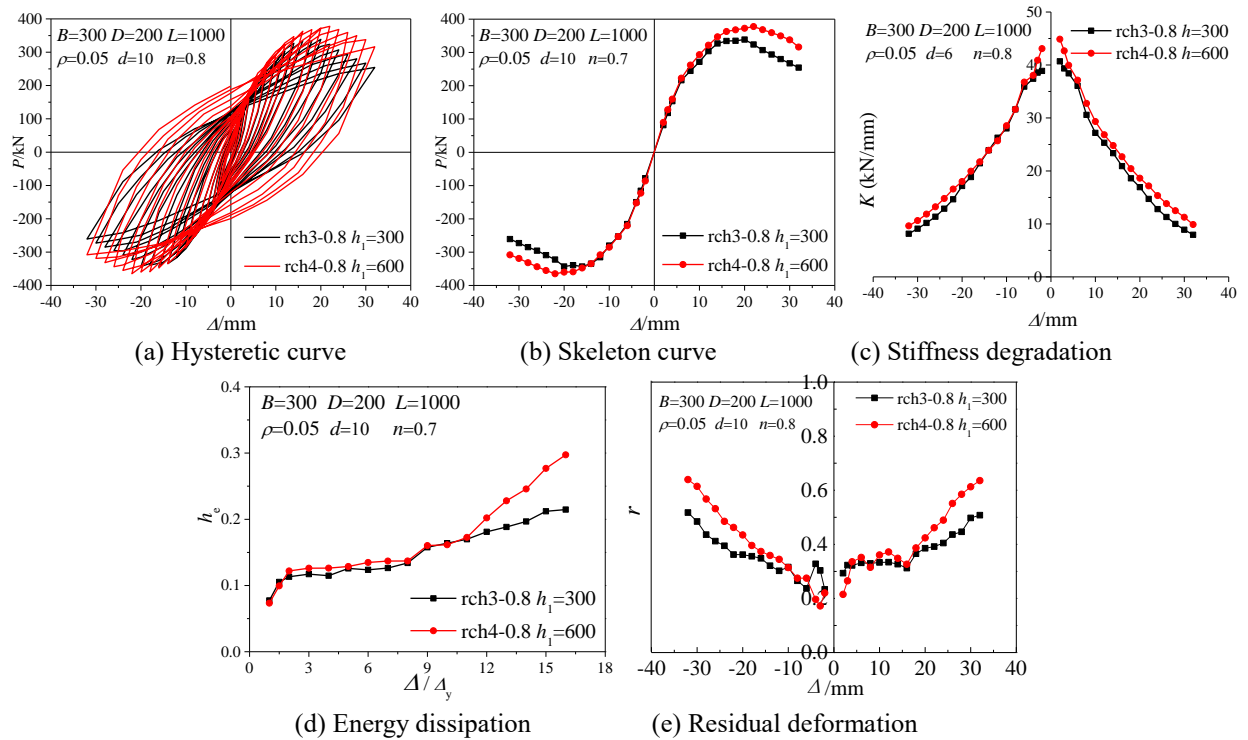
308

309

310 by 6.0%, 18.1%, 8.0% respectively. Besides, stiffness degrades more gently. Furthermore, h_e and r are
 311 generally increased at the same loading displacement, which indicates that increasing h_1 can effectively
 312 improve the seismic behavior of specimens. Similarly, compared to specimen rch3-0.8, the P , DI , K_1 of
 313 rch4-0.8 are improved by 10.1%, 12.4%, 10.5%, respectively.



314
315
316
317
318 **Fig.11. Influence of height of terminal stirrup region on hysteresis behavior when n is 0.7**



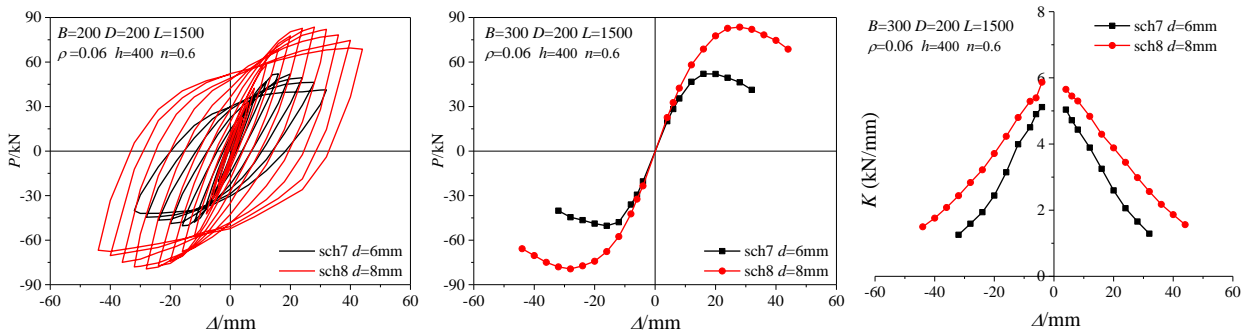
319
320
321
322
323
324
325 **Fig.12. Influence of height of terminal stirrup region on hysteresis behavior when n is 0.8**

326 4.4. Effect of equivalent stirrup ratio

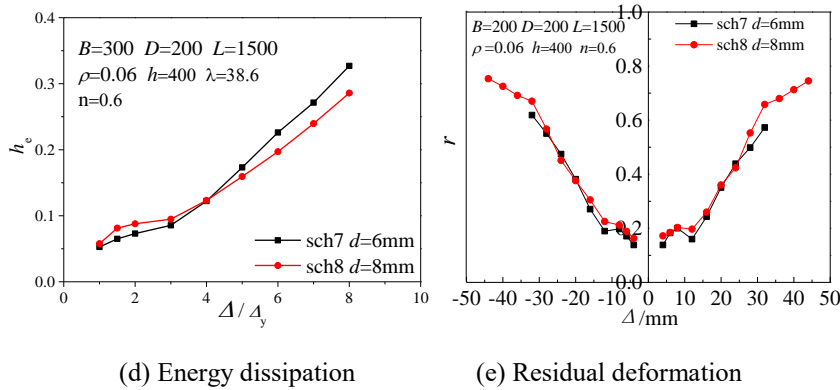
326 Fig. 13 compares the effect of equivalent stirrup ratio ρ_{sa} on the hysteresis behavior when n is 0.6 and
 327 the stirrups range is 400mm ($2B$). The diameter d_s of the stirrups are 6mm and 8mm, and the yield strength
 328 f_s of the stirrups are 285MPa and 504MPa, respectively. Thus the ρ_{sa} increases from 0.45% to 1.42% and

329 increased by 215.6%. It can be seen from Fig. 13 and Table 1 that the hysteresis loop is plumper and the
 330 skeleton curve declines more slowly when the ρ_{sa} is increased. Compared to sch7, the P , DI , K_1 of sch8
 331 are increased from 52.03 kN, 2.85, 5.12 kN/mm to 83.54 kN, 3.02, 5.87 kN/mm. On the whole, the 3 indexes are
 332 improved by 60.6%, 10.2%, 8.0% respectively. In addition, stiffness degrades more gently. At the early stage
 333 of loading, the difference of h_e between sch7 and sch8 is not obvious. But at the late stage of loading, the
 334 h_e of sch8 was significantly less than h_e of sch7. This is because the horizontal load of sch8 declines slower than
 335 that of sch7, and the $S_{(OBE+ODF)}$ in the formula (4) is still larger, resulting in a smaller h_e . However, there is little
 336 difference between the r of the 2 specimens. The above analysis contributes that increasing ρ_{sa} can effectively
 337 improve the seismic behavior of the specimen.

338 Similarly, Fig. 14 compares the effect of ρ_{sa} on the hysteresis behavior when n is 0.8 and the stirrups
 339 range is 600mm ($2B$). The diameter d_s of the stirrups are 8mm and 10mm, and the yield strength f_s of the
 340 stirrups are 444MPa and 532MPa, respectively. Thus the ρ_{sa} increases from 1.49% to 2.79% and increased
 341 by 87.2%. Compared to specimen rch2-0.8, the P , DI , K_1 of rch4-0.8 are improved by 14.9%, 12.4%, 5.5%,
 342 respectively.

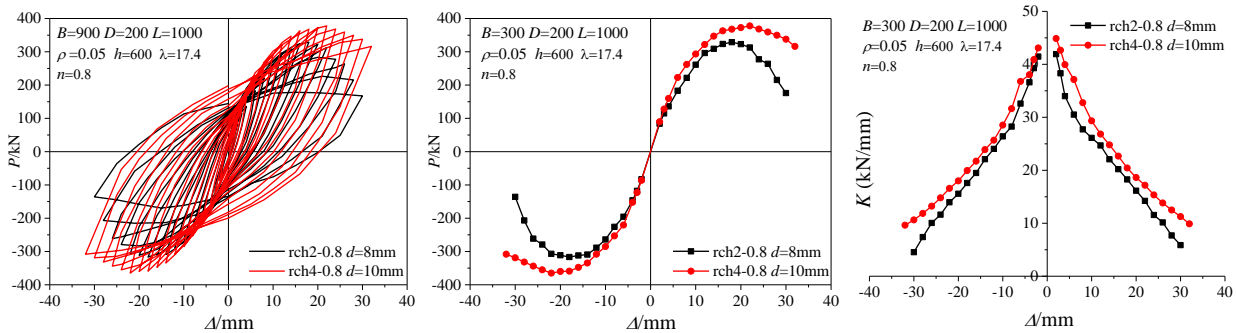


343 (a) Hysteretic curve (b) Skeleton curve (c) Stiffness degradation

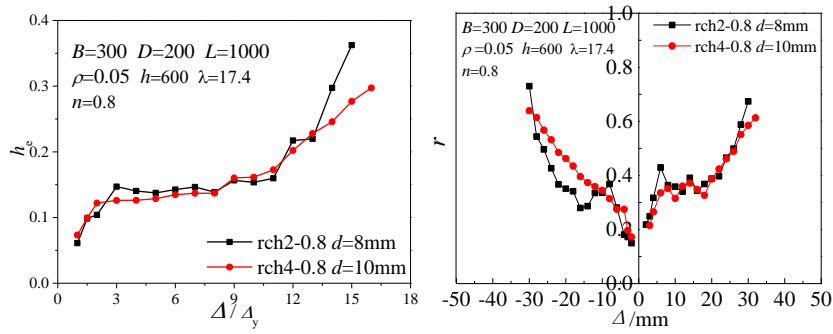


344 (d) Energy dissipation (e) Residual deformation

345 **Fig.13. Influence of equivalent stirrup ratio on hysteresis behavior when n is 0.6**



346 (a) Hysteretic curve (b) Skeleton curve (c) Stiffness degradation

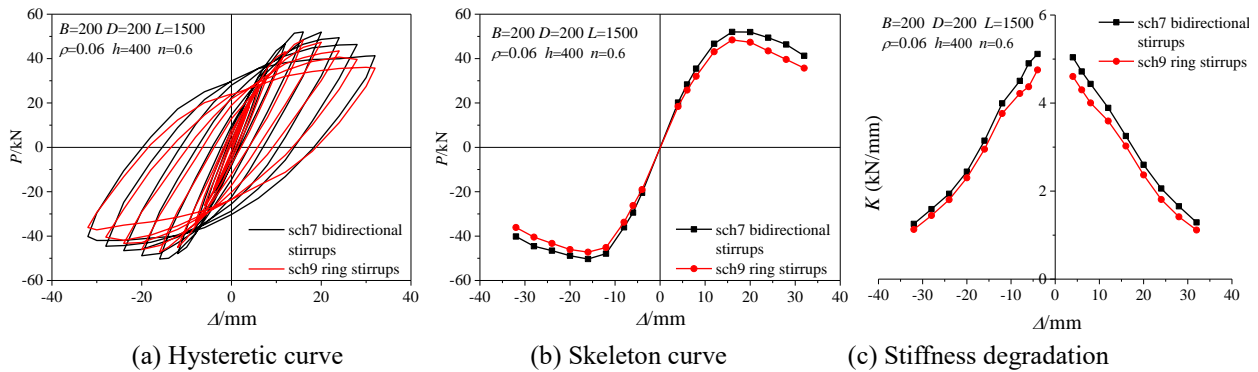


(d) Energy dissipation (e) Residual deformation

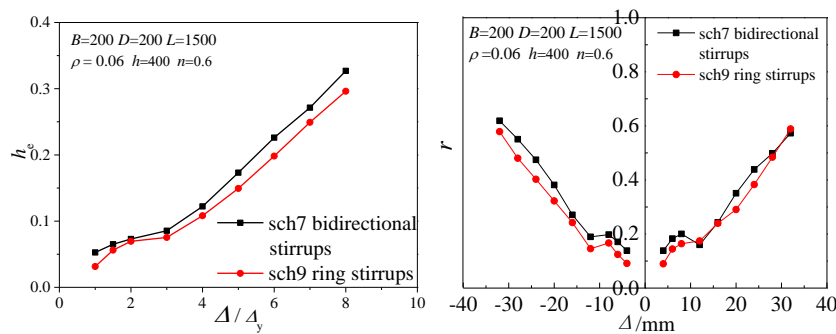
Fig.14. Influence of equivalent stirrup ratio on hysteresis behavior when n is 0.8

4.5. Effect of stirrup forms

Fig. 15 compares the effect of stirrup forms on the hysteresis behavior when n is 0.6 and the stirrups range is 400mm ($2B$). The ρ_{sa} of sch9 (ring stirrups) and sch7 (bidirectional stirrups) are 0.73% and 0.45% respectively, reduced by 38.4%. However, compared to sch9, the hysteresis loop of sch7 is plumper and its skeleton curve tends to decline more slowly. In addition, The P , DI , K_1 of sch7 are increased from 48.40 kN, 2.38, 4.8 kN/mm to 52.03 kN, 2.85, 5.1 kN/mm. On the whole, the 3 indexes are improved by 7.5%, 19.7%, 6.3%, respectively. Furthermore, h_e and r of sch7 are greater than those of sch9, which state that the seismic behavior of specimen with bidirectional stirrups is superior to specimen with ring stirrups.



(a) Hysteretic curve (b) Skeleton curve (c) Stiffness degradation



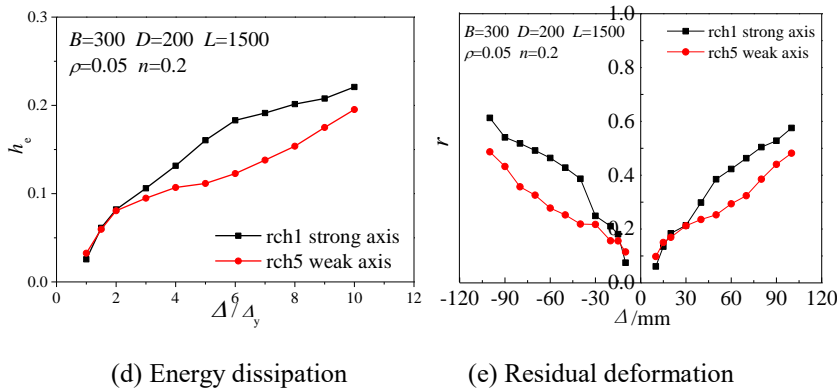
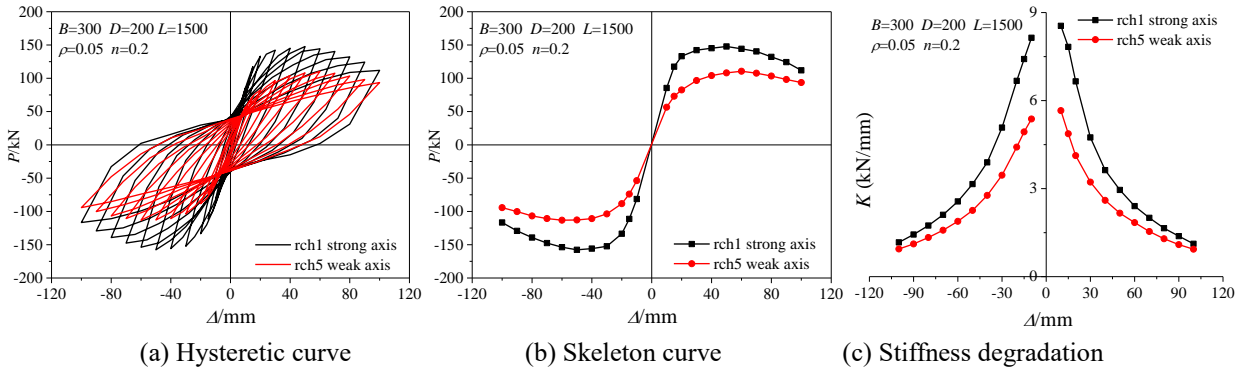
(d) Energy dissipation (e) Residual deformation

Fig.15. Influence of stirrup form on hysteresis behavior

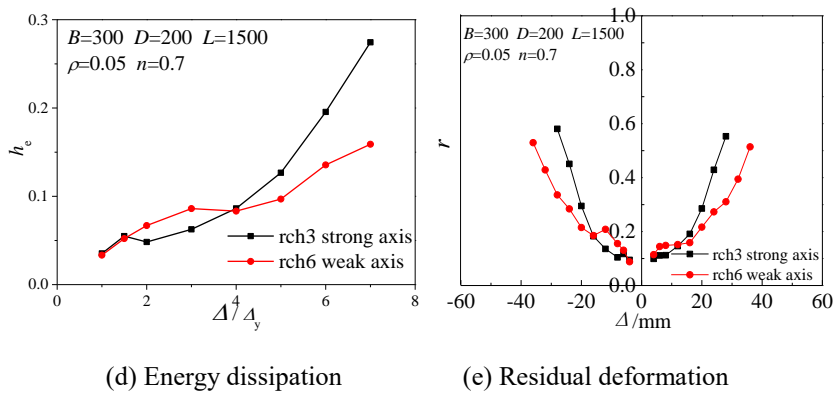
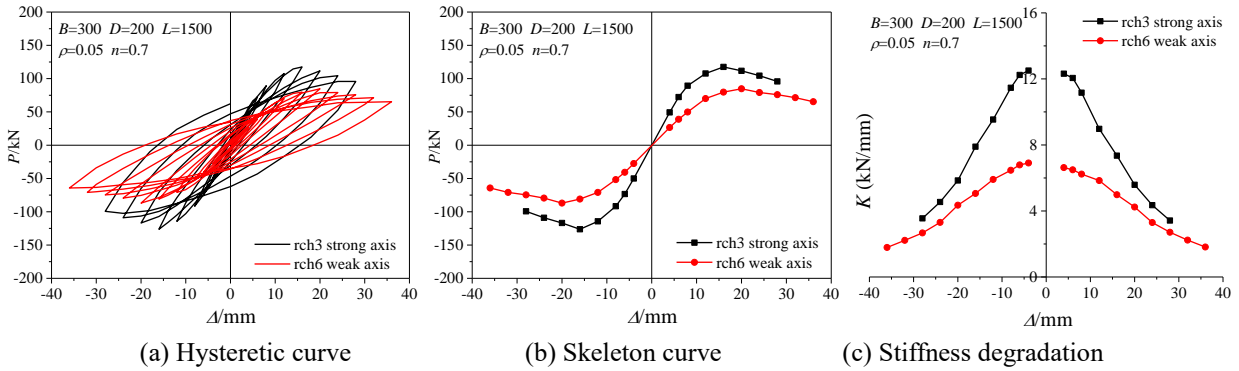
4.6. Effect of loading direction

Fig. 16 and Fig. 17 show the difference of loading direction on the hysteretic behavior of the specimens, when n are 0.2 and 0.7, respectively. It is explained from Fig. 16, Fig. 17 and Table 1 that the hysteresis curve of strong axis loading is plumper than that of weak axis loading. In addition, P , K of each

372 hysteresis loop, h_e and r of strong axis loading are larger than those of weak axis loading. Compared to
 373 specimens rch5, rch6, the DI of rch1, rch3 are decreased from 4.83, 2.48 to 4.54, 2.26, decreased by 6.0%,
 374 8.9%. The difference between DI of them is not significant, indicating that the loading direction has little
 375 influence on the ductility of rectangular SCFT specimens.



378
379
380 **Fig.16. Influence of loading direction on hysteresis behavior when n is 0.2**



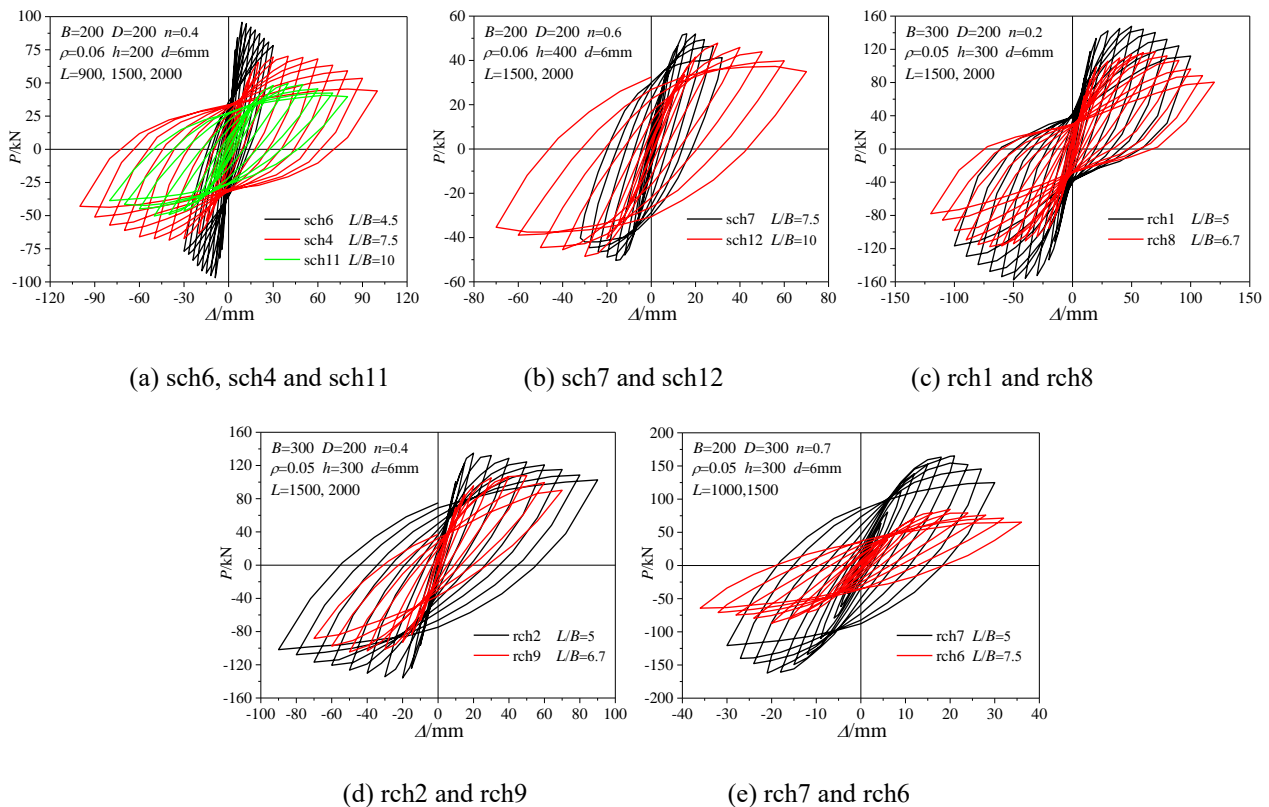
383
384
385
386 **Fig.17. Influence of loading direction on hysteresis behavior when n is 0.7**

387 **4.7. Effect of height-length ratio (L/B)**

388 Fig. 18 compares the influence of different height-length ratios (L/B) on the hysteresis curve of
 389 specimens. As seen from Fig. 18 and Table 1, the higher the L/B is, the less the P and the K_1 are, the faster
 390 the horizontal load decreases, the worse the seismic behavior and the hysteresis loops are slightly pinched.
 391 Compared to sch6, the L/B of sch4 and sch11 are increased from 4.5 to 7.5, 10, increased by 66.7%,
 392 122.0%, respectively. But the DI decreases from 4.71 to 4.38, 4.08, decreases by 7.0%, 13.4%, respectively.
 393 Similarly, compared to sch7, the L/B of sch12 is increased from 7.5 to 10, increased by 33.3%, respectively.
 394 The DI decreases from 2.85 to 2.63, decreases by 7.7%. What's more, compared to rch1, rch2 and rch7,
 395 the L/B of rch8, rch9 and rch6 are increased from 5, 5, 5 to 6.7, 6.7, 7.5, increased by 34.0%, 34.0%, 50%
 396 respectively. The DI decreases from 4.54, 4.27, 2.75 to 4.12, 3.85, 2.47, decreases by 9.3%, 9.8%, 10.2%.
 397 It can be found that when the L/B increases significantly, the DI of the rectangular SCFT decreases very
 398 finitely.

399

400



401

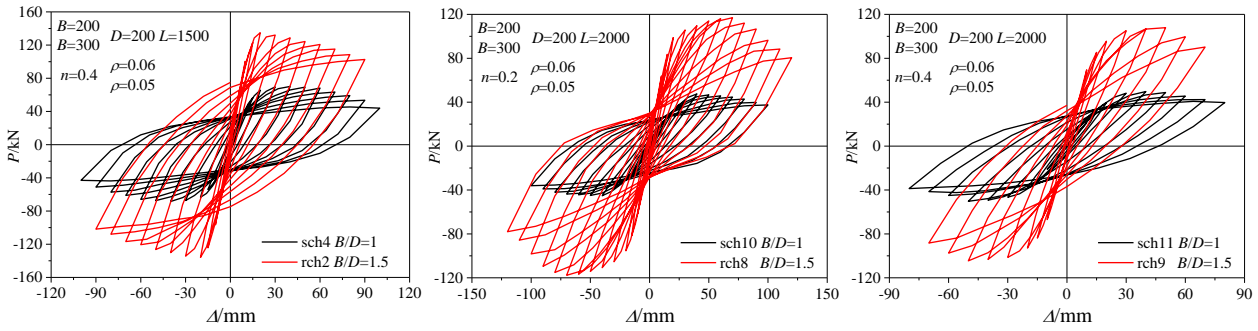
402

403

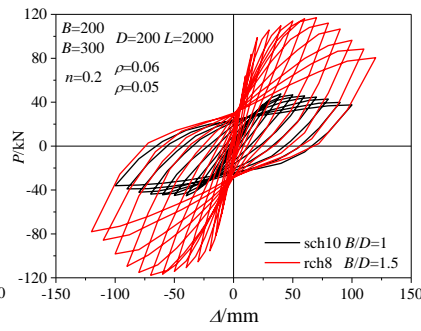
404

405 **4.8. Effect of length-width ratio (B/D)**

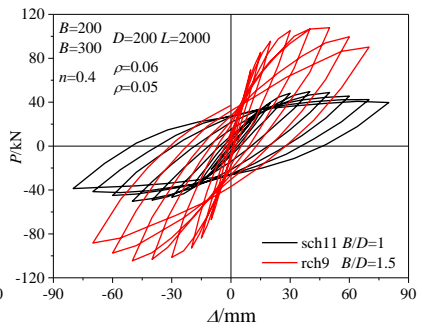
406 Fig. 19 and Fig. 20 compare the effect of two length-width ratios $B/D=1$ (square SCFT) and $B/D=1.5$
 407 (rectangular SCFT) on hysteresis curve and energy dissipation, respectively. It is indicated from Fig. 19,
 408 Fig. 20 and Table 1 that when $B/D=1.5$, both the K and the P are larger. But the hysteresis loops
 409 demonstrate slightly pinched. On the contrary, when $B/D=1.0$, both the K and the P are smaller. But the
 410 hysteresis loops are plumper without pinched. At the same displacement, h_e of square SCFT is greater than
 411 that of rectangular SCFT which indicates that the energy dissipation capacity of square SCFT is superior to
 412 that of rectangular SCFT. Compared to square SCFT rch3, sch10, sch11 and sch12, the DI of rch2, rch8,
 413 rch9 and rch10 are decreased from 4.38, 4.62, 4.08 and 3.63 to 4.27, 4.22, 3.85 and 3.39, decreased by 2.5%,
 414 8.7%, 5.6% and 6.6% respectively. It states that the influence of length-width ratio on the DI of these
 415 rectangular SCFT is tiny.



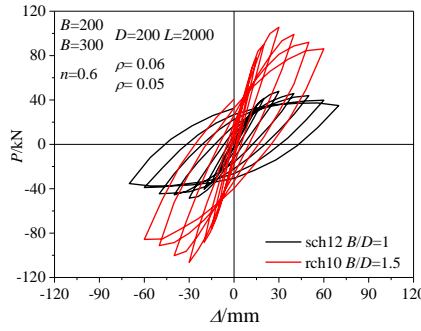
(a) sch4 and rch2



(b) sch10 and rch8

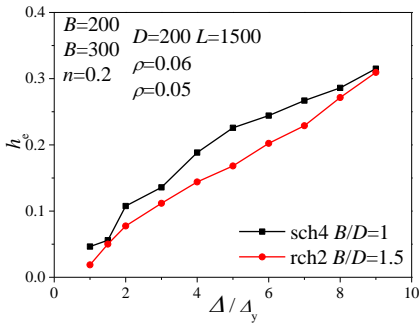


(c) sch11 and rch9

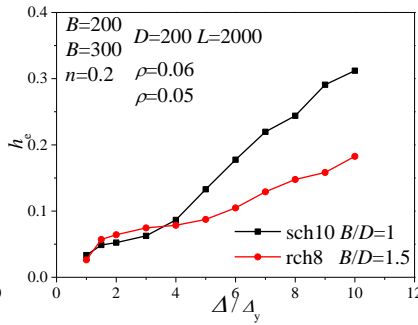


(d) sch12 and rch10

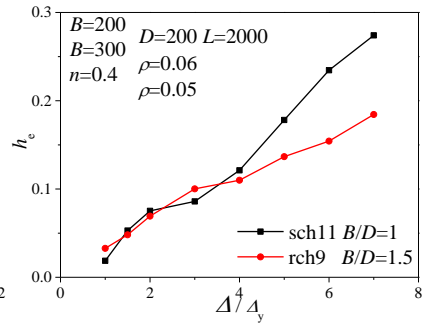
Fig.19. Influence of length-width ratio on hysteresis curve



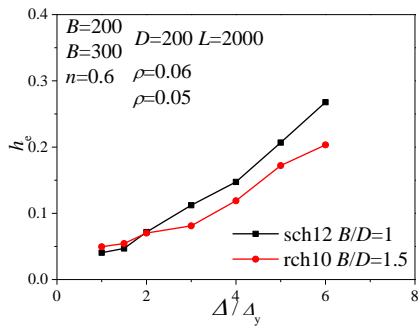
(a) sch4 and rch2



(b) sch10 and rch8



(c) sch11 and rch9



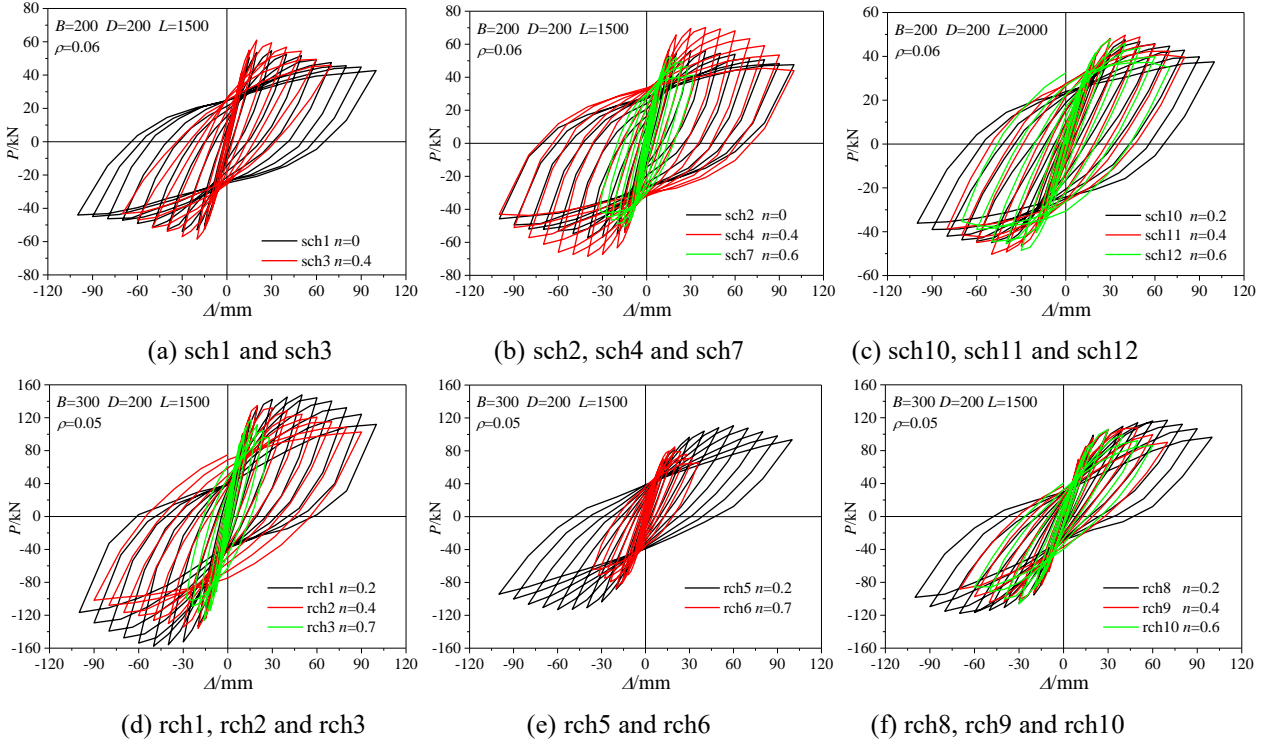
(d) sch12 and rch10

Fig.20. Influence of length-width ratio on equivalent viscous damping index

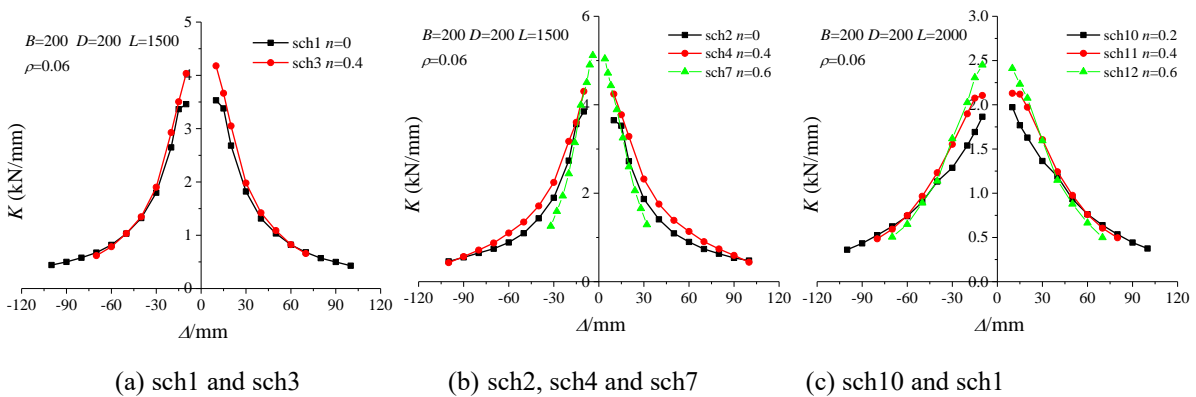
4.9. Effect of axial compression ratio (n)

Figs 21, 22, 23, 24 compared the effects of different n on the hysteretic curves, stiffness degradation, DI and h_e . With the increase of n , the initial stiffness of the specimens is generally increased, but descends steeper and the DI is obviously reduced. The DI of rectangular SCFT with small n or medium n is generally larger than 3, indicating that the ductility of the specimens is good and can meet the seismic design requirements. Among all specimens, the DI of rch3 is the least, which is 2.26 due to its low ρ_{sa} and

433 high value of n ($n=0.7$). Based on the "General yield bending moment method", the failure displacement Δ_u
 434 of rch3 is 26.0mm. Accordingly, the maximum displacement angle (Δ_u/L) is 1/58, which cannot meet the
 435 limit value 1/50 of relevant standards [28, 29]. Therefore it is necessary to increase the ρ_{sa} and conduct the
 436 corresponding experimental study. When n increases from 0 to 0.4 or from 0.2 to 0.4, the P of the
 437 specimens is generally increased. However, when n is further increased to 0.6 or 0.7, the P is decreased,
 438 while the K_1 of the specimen is generally increased. With the increase of the n , the hysteresis loop is
 439 plumper and h_e is generally increased, indicating that the energy dissipation capacity is enhanced. For
 440 reinforced concrete members in seismic field, the h_e values is approximately 0.1~0.2 [30]. By contrast, the
 441 h_e values of the SCFT specimens in this test range from 0.15 to 0.4, which demonstrate that the energy
 442 dissipation capacity of SCFT is better than that of reinforced concrete members.

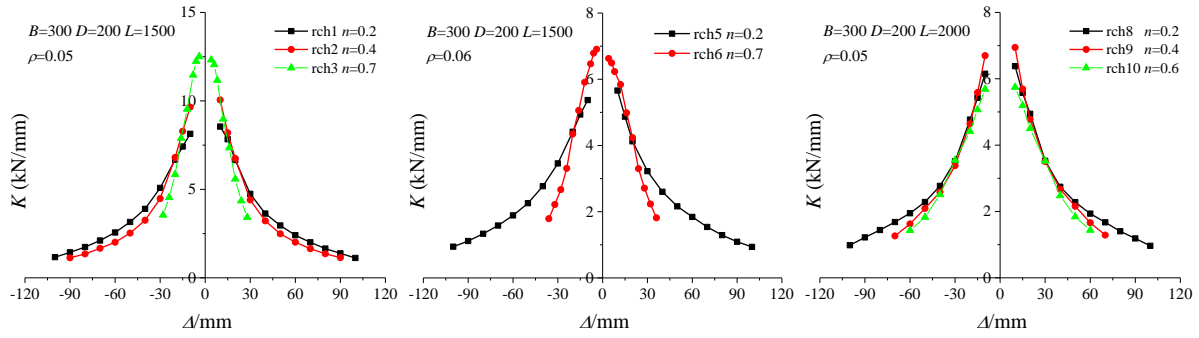


445 **Fig.21. Influence of n on hysteresis curve**



448

449

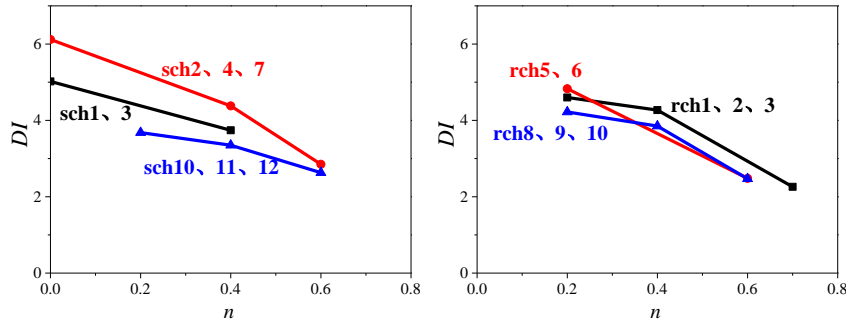


(d) rch1, rch2 and rch3

(e) rch5 and rch6

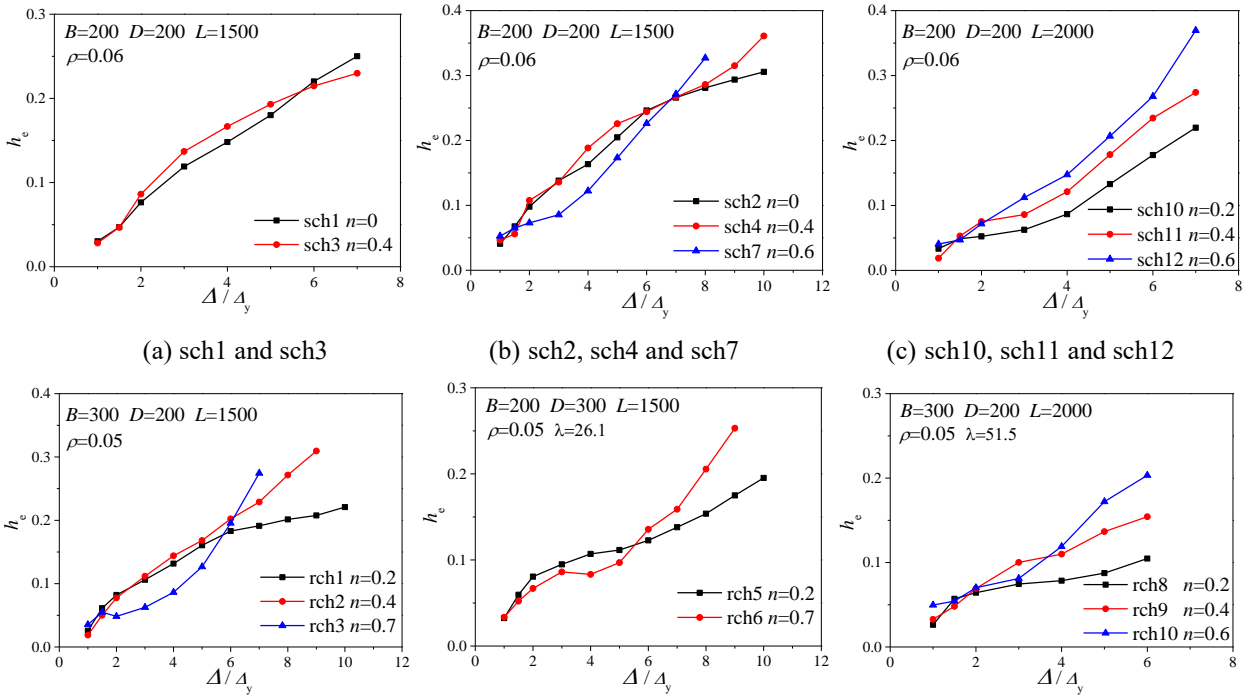
(f) rch8, rch9 and rch10

Fig.22. Influence of n on stiffness degradation



(a) $DI-n$ of square specimens (b) $DI-n$ of rectangular specimens

Fig.23. $DI-n$ relationship curve



(a) sch1 and sch3

(b) sch2, sch4 and sch7

(c) sch10, sch11 and sch12

(d) rch1, rch2 and rch3

(e) rch5 and rch6

(f) rch8, rch9 and rch10

Fig.24. Influence of n on equivalent viscous damping index

4.10. Effect of sliding support

Fig. 25 compares the effect of sliding support on the hysteresis behavior when n is 0.4 and the stirrups range is 200mm (B). Because the friction between the jack and the top plate is eliminated due to the sliding support, the skeleton curve of sch3 declines more gently and its stiffness degrade more slowly than sch5.

466 Also, we can see from Table 1 that the DI of sch3 increased from 3.35 to 3.74, increased by 11.6%. However,
 467 friction leads the K_1 of sch5 increase from 4.11kN/mm to 4.96kN/mm and the P of sch5 increased from
 468 61.02kN to 66.81kN, increased by 20.7% and 9.5%, respectively. In addition, the hysteresis curve of sch5
 469 is plumper and its maximum h_e increased from 0.23 to 0.34, increased by 47.8%.The above results
 470 contribute that the impact of friction cannot be ignored in the test , and the sliding support can ensure the
 471 experimental data more accurate.

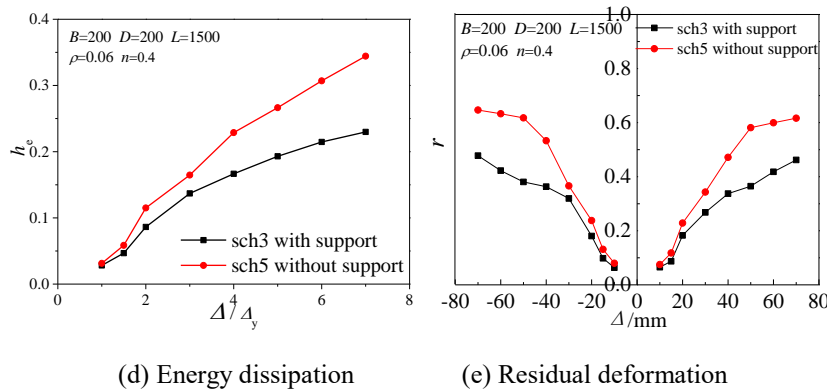
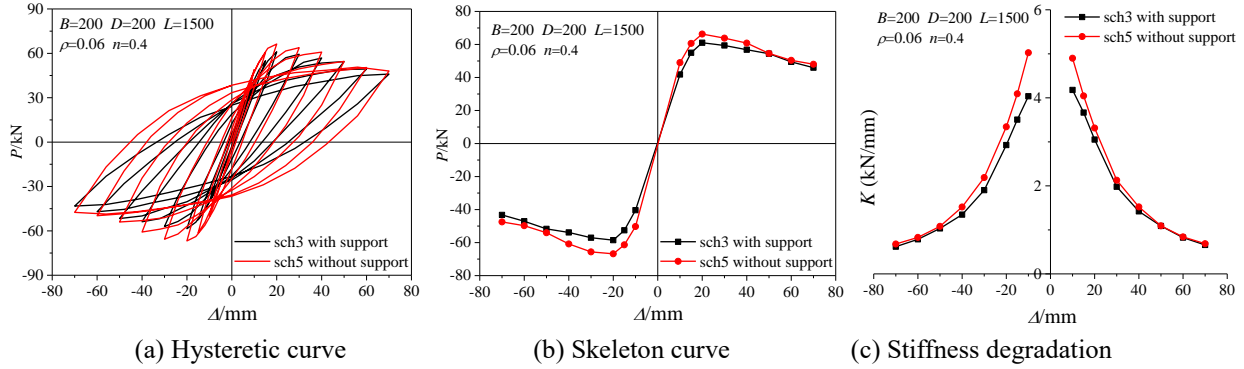


Fig.25. Influence of sliding support on hysteresis behavior

5. Conclusions

479 This paper presents a pseudo-static experimental study on the seismic behavior of stirrup-confined
 480 concrete-filled rectangular steel tubular columns. The experimental program consists of 26 specimens with
 481 consideration of with or without stirrups, height of terminal stirrup region, equivalent stirrup ratio, loading
 482 direction, and axial compression ratio etc. Based on the results of failure mode, strain ratio, ultimate
 483 bearing capacity ductility, stiffness degradation, energy dissipation, and residual deformation, the
 484 following conclusions can be drawn:

485 (1) Under axial pressure and horizontal low cyclic load, the specimens are failed mainly by buckling of
 486 the steel tubes, crush of the core concrete and fracture of the stirrups. The equivalent viscous damping index
 487 of the specimens ranges from 0.15 to 0.4, which demonstrates that they have good seismic energy
 488 dissipation capacity.

489 (2) The maximum strain ratio of typical specimens is more than 0.5, showing that the steel tube exerts
 490 a good confinement on the core concrete. The axial pressure can increase the confining effect of steel tube
 491 to the core concrete. In addition, the stirrups can directly confine the core concrete, and reduce the
 492 maximum strain ratio of the steel tube.

493 (3) When the axial compression ratio is larger, the bidirectional stirrups can delay local buckling of
 494 steel tube, improve the confinement effect on the core concrete effectively, and thus increase the ultimate
 495 bearing capacity and ductility index, so as to significantly improve the seismic behavior of the rectangular
 496 SCFT columns. At the same axial compression ratio, increasing height of terminal stirrup region or

497 increasing equivalent stirrup ratio can also effectively improve the seismic behavior of the specimens.

498 (4) The ultimate bearing capacity of the rectangular SCFT of strong axis loading is distinctly greater
499 than that of weak axis loading, but there is no obvious difference between their ductility. When the
500 height-length ratio and length-width ratio increases, the ductility DI decreases very limited.

501

502 **Acknowledgment**

503 This research work was financially supported by the National Key Research Program of China, Grant
504 No. 2017YFC0703404.

505

506 **References**

- 507 [1] X. Chang, C.K. Huang, Y.J. Chen, Mechanical performance of eccentrically loaded pre-stressing
508 concrete filled circular steel tube columns by means of expansive cement, *Eng. Struct.* 31 (11) (2009)
509 2588-2597.
- 510 [2] X. Chang, L. Fu, H.B. Zhao, Y.C. Song, Behaviors of axially loaded circular concrete-filled steel tube
511 (CFT) stub columns with notch in steel tubes, *Thin-Walled Struct.* 73 (12) (2013) 273-280.
- 512 [3] X. Chang, X.L. Luo, C.X. Zhu, C.A. Tang, Analysis of circular concrete-filled steel tube (CFT)
513 support in high ground stress conditions, *Tunn. Undergr. Space Technol.* 43 (3) (2014) 41-48.
- 514 [4] M.F. Hassanein, O.F. Kharoob, Compressive strength of circular concrete-filled double skin tubular
515 short columns, *Thin-Walled Struct.* 77 (4) (2014) 165-173.
- 516 [5] M.F. Hassanein, O.F. Kharoob, L. Gardner, Behaviour and design of square concrete-filled double
517 skin tubular columns with inner circular tubes, *Eng. Struct.* 100 (10) (2015) 410-424.
- 518 [6] Y.S. Huang, Y.L. Long, J. Cai, Ultimate strength of rectangular concrete-filled steel tubular (CFT)
519 stub columns under axial compression, *Steel Compos. Struct.* 8 (2) (2008) 115-128.
- 520 [7] B. Evirgen, A. Tuncan, K. Taskin, Structural behavior of concrete filled steel tubular sections
521 (CFT/CFSt) under axial compression, *Thin-Walled Struct.* 80 (7) (2014) 46-56.
- 522 [8] X.S. Qu, Z.H. Chen, G.J. Sun, Axial behaviour of rectangular concrete-filled cold-formed steel tubular
523 columns with different loading methods, *Steel Compos. Struct.* 18 (1) (2015) 71-90.
- 524 [9] Y.S. Du, Z.H. Chen, M.X. Xiong, Experimental behavior and design method of rectangular
525 concrete-filled tubular columns using Q460 high-strength steel, *Constr. Build. Mater.* 125 (30) (2016)
526 856-872.
- 527 [10] A.H. Varma, J.M. Ricles, R. Sause, L.W. Lu, Seismic behavior and design of high-strength square
528 concrete-filled steel tube beam columns, *J. Struct. Eng.* 130 (2) (2004) 169-179.
- 529 [11] J.P. Liu, X.H. Zhou, S.M. Zhang, Seismic behaviour of square CFT beam-columns under biaxial
530 bending moment, *J. Constr. Steel Res.* 64 (12) (2008) 1473-1482.
- 531 [12] L.H. Han, Y.F. Yang, Z. Tao, Concrete-filled thin-walled steel SHS and RHS beam-columns subjected
532 to cyclic loading, *Thin-Walled Struct.* 41 (9) (2003) 801-833.
- 533 [13] X.Y. Mao, Y. Xiao, Seismic behavior of confined square CFT columns, *Eng. Struct.* 28 (10) (2006)
534 1378-1386.
- 535 [14] M.C. Zhu, J.X. Liu, Q.X. Wang, Experimental study of square steel tubes filled with steel-reinforced
536 high-strength concrete. *China Civil Eng. J.* 44 (7) (2011) 55-63. (in Chinese)
- 537 [15] Y.C. Zhang, C. Xu, X.Z. Lu, Experimental study of hysteretic behaviour for concrete-filled square
538 thin-walled steel tubular columns, *J. Constr. Steel Res.* 63 (3) (2007) 162-175.
- 539 [16] Y.T. Wang, J. Cai, Y.L. Long, Hysteretic behavior of square CFT columns with binding bars, *J. Constr.*
540 *Steel Res.* 131 (4) (2017) 162-175.
- 541 [17] F.X. Ding, D.R. Lu, Y. Bai, Q.S. Zhou, N. M, Z.W. Yu, G.S. Jiang, Comparative study of square
542 stirrup-confined concrete-filled steel tubular stub columns under axial loading. *Thin-Walled Struct.* 98

- 543 (1) (2016) 443-453.
- 544 [18] F.X. Ding, L. Fu, X.M. Liu, J. Liu, Mechanical performances of track-shaped rebar stiffened
545 concrete-filled steel tubular (SCFRT) stub columns under axial compression. *Thin-Walled Struct.* 99
546 (2) (2016) 168-181.
- 547 [19] F.X. Ding, X.Y. Ying, L.C. Zhou, Z.W. Yu, Unified calculation method and its application in
548 determining the uniaxial mechanical properties of concrete. *Front. Archit. Civ. Eng. China* 5(3) (2011)
549 381-393.
- 550 [20] GB 50017-2003. Code for design of steel structures. China Planning Press, Beijing, 2003.
- 551 [21] GB/T50081-2002. Standard for method of mechanical properties on ordinary concrete. China
552 Building Industry Press, Beijing, 2002.
- 553 [22] GB/T228-2002. Metallic materials-tensile testing at ambient temperatures. Standards Press of China,
554 Beijing, 2002.
- 555 [23] JGJ/T 101-2015. Specification for seismic test of buildings. Building Industry Press, Beijing, 2015.
- 556 [24] Z.W. Yu, F.X. Ding, C.S. Cai, Experimental behavior of circular concrete-filled steel tube stub
557 columns, *J. Constr. Steel. Res.* 63 (2) (2007) 165–174.
- 558 [25] J.Y. Xue, H. Ma, Y. Liu, Experimental study on seismic performance of steel reinforced recycled
559 concrete columns under low-cyclic reversed loading, *China Civil Eng. J.* 47(1) (2014) 36-46.
- 560 [26] J.G. Nie, J.S. Fan, X.G. Liu, Y. Huang, Comparative study on steel plate shear walls used in a
561 high-rise building, *J. Struct. Eng.* 139 (1) (2013) 85-97.
- 562 [27] J.G. Nie, K. Qing, R. Liu, Experimental study on seismic behavior of connections composed of
563 concrete-filled square steel tubular columns and steel-concrete composite beams with interior
564 diaphragms, *China Build. Struct. J.* 27 (4) (2006) 1-9.
- 565 [28] GB50936-2014. Technical code of concrete filled steel tubular structures.: Building Industry Press,
566 Beijing, 2014.
- 567 [29] CECS159:2004. Technical specification for structures with concrete-filled rectangular steel tube
568 members. China Planning Press, Beijing, 2004.
- 569 [30] M. Eduardo, R.G. Jorge, Evaluation of approximate methods to estimate maximum inelastic
570 displacement demands. *Earthquake Eng. Struct. Dyn.* 31 (3) (2002) 539-560.